Article

Fluorescent bicolour sensor for low-background neutrinoless double β decay experiments

Iván Rivilla[1], Borja Aparicio[2], Juan M. Bueno[3], David Casanova[1,4], Claire Tonnelé[1], Zoraida Freixa[4,5], Pablo Herrero[1], Celia Rogero[1,6], José I. Miranda[7], Rosa M. Martínez-Ojeda[3], Francesc Monrabal[1,4], Beñat Olave[8], Thomas Schäfer[4,8], Pablo Artal[3], David Nygren[9], Fernando P. Cossío[1,2 ✉] & Juan J. Gómez-Cadenas[1,4 ✉]

Observation of the neutrinoless double β decay is the only practical way to establish that neutrinos are their own antiparticles[1]. Because of the small masses of neutrinos, the lifetime of neutrinoless double β decay is expected to be at least ten orders of magnitude greater than the typical lifetimes of natural radioactive chains, which can mimic the experimental signature of neutrinoless double β decay[2]. The most robust identification of neutrinoless double β decay requires the definition of a signature signal—such as the observation of the daughter atom in the decay—that cannot be generated by radioactive backgrounds, as well as excellent energy resolution. In particular, the neutrinoless double β decay of ^{136}Xe could be established by detecting the daughter atom, ^{136}Ba^{2+}, in its doubly ionized state[3–8]. Here we demonstrate an important step towards a 'barium-tagging' experiment, which identifies double β decay through the detection of a single Ba^{2+} ion. We propose a fluorescent bicolour indicator as the core of a sensor that can detect single Ba^{2+} ions in a high-pressure xenon gas detector. In a sensor made of a monolayer of such indicators, the Ba^{2+} dication would be captured by one of the molecules and generate a Ba^{2+}-coordinated species with distinct photophysical properties. The presence of such a single Ba^{2+}-coordinated indicator would be revealed by its response to repeated interrogation with a laser system, enabling the development of a sensor able to detect single Ba^{2+} ions in high-pressure xenon gas detectors for barium-tagging experiments.

Double β decay (ββ) is a very rare nuclear transition in which a nucleus with Z protons decays into a nucleus with Z + 2 protons and the same mass number A. The decay can occur only if the initial nucleus is less strongly bound than the final nucleus, and both of them are more strongly bound than the intermediate Z + 1 nucleus. Two decay modes are usually considered: (i) The standard two-neutrino mode (ββ2ν), consisting of two simultaneous β decays, $(Z, A) \rightarrow (Z + 2, A) + 2e^- + 2\bar{\nu}_e$ (e^-, electron; $\bar{\nu}_e$, electron antineutrino), which has been observed in several isotopes with typical half-lives in the range 10^{18}–10^{21} yr; and (ii) The neutrinoless mode (ββ0ν), $(Z, A) \rightarrow (Z + 2, A) + 2e^-$, which violates lepton-number conservation and can occur if and only if neutrinos are Majorana particles[1]—that is, identical to their antiparticles. An unambiguous observation of such a decay would have deep implications in particle physics and cosmology, offering a mechanism for leptogenesis[9] and a potential explanation for the cosmic asymmetry between matter and antimatter[10]. Furthermore, Majorana neutrinos could provide an explanation of the smallness of the neutrino mass compared with those of other leptons, through the so-called see-saw mechanism[11–13].

Double β decay (ββ) experiments have been searching for ββ0ν in several isotopes for more than half a century, without finding clear evidence of a signal so far. The current best lower limit on the lifetime ($T_{1/2}^{0\nu}$) of the ββ0ν processes has been obtained for the isotope ^{136}Xe, for which $T_{1/2}^{0\nu} > 10^{26}$ yr (ref. [14]). Two other isotopes, ^{76}Ge and ^{130}Te, have also been studied with similar sensitivities, yielding no evidence of ββ0ν decay[15,16]. A new generation of ββ0ν experiments will aim to improve the sensitivity to $T_{1/2}^{0\nu}$ by at least one, and eventually two, orders of magnitude[17]. These searchers will require very large exposures, measured in ton-years, but even more importantly, a greatly enhanced capability to suppress backgrounds from false events. The most obvious background to ββ0ν is the ββ2ν decay, which also produces two electrons and the same daughter atom as the neutrinoless mode while having a

[1]Donostia International Physics Center (DIPC), San Sebastián/Donostia, Spain. [2]Department of Organic Chemistry I, University of the Basque Country (UPV/EHU), Centro de Innovación en Química Avanzada (ORFEO-CINQA), San Sebastián/Donostia, Spain. [3]Laboratorio de Óptica (LOUM) & Centro de Investigación en Óptica y Nanofísica (CiOyN), University of Murcia, Murcia, Spain. [4]Ikerbasque, Basque Foundation for Science, Bilbao, Spain. [5]Department of Applied Chemistry, Faculty of Chemistry, University of the Basque Country (UPV/EHU), San Sebastián/Donostia, Spain. [6]Materials Physics Center CFM (CSIC-UPV/EHU), San Sebastián/Donostia, Spain. [7]SGIker NMR Facility, University of the Basque Country (UPV/EHU), San Sebastián/Donostia, Spain. [8]NanoBioSeparations Group, POLYMAT, University of the Basque Country (UPV/EHU), San Sebastián/Donostia, Spain. [9]Department of Physics, University of Texas at Arlington, Arlington, TX, USA. ✉e-mail: fp.cossio@ehu.es; jjgomezcadenas@dipc.org

Article
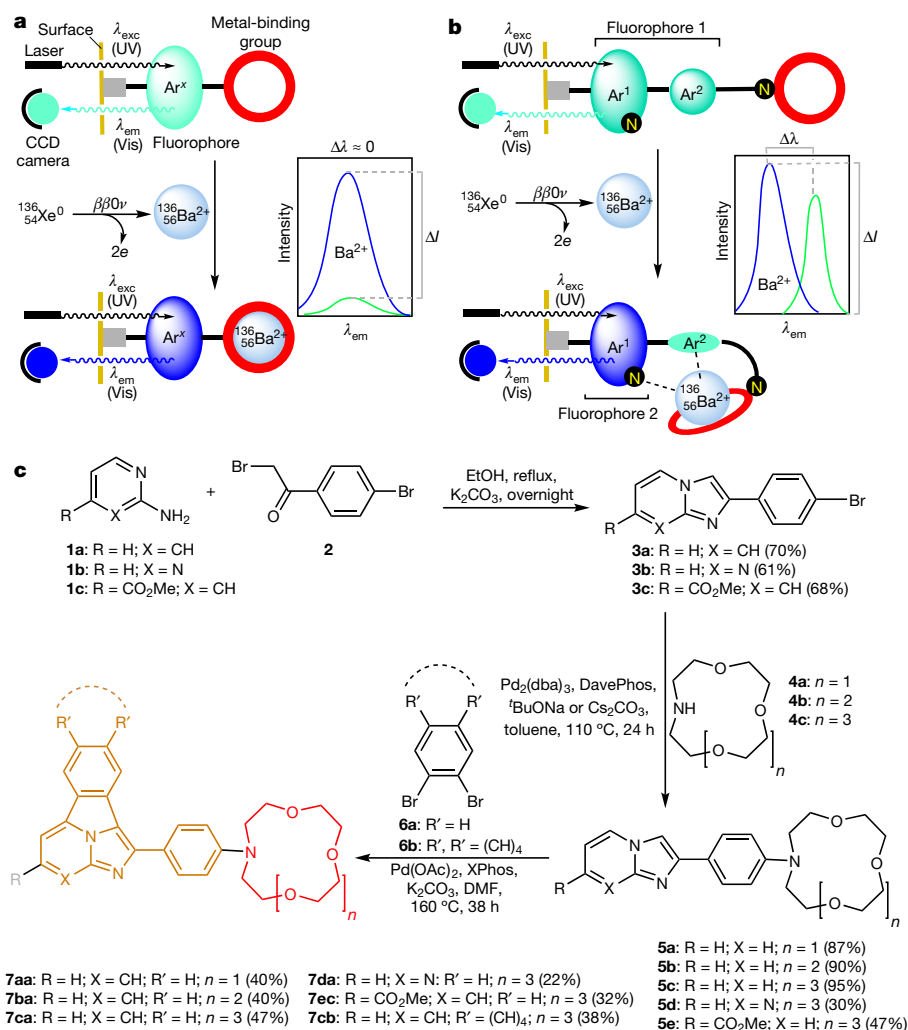
Fig. 1 | Design and synthesis of a family of FBIs. a, Components of a fluorescent monocolour indicator. UV, ultraviolet; Vis, visible; CCD, charge-coupled device; em, emission; exc, excitation; Ar^x, aryl or heteroaryl group (monocyclic or polycyclic). **b**, Components of an FBI analogue, showing the coupling–decoupling between the fluorophore and the metal-binding group. The respective expected fluorescent emission spectra are also shown. The blue and green lines in the graphs in **a**, **b** represent the emission spectra in chelated and unchelated indicators, respectively. The different behaviour of the two types of fluorescent indicator is shown: in a monocolour indicator, the increase in emission intensity after cation complexation (ΔI) is produced at the same wavelength as the unchelated fluorophore ($\Delta\lambda \approx 0$), whereas in the case of an FBI, the difference ΔI is produced at a different wavelength ($\Delta\lambda \neq 0$).

The possible participation of nitrogen heteroatoms and the rotation of one aryl group (Ar^2) are also highlighted. **c**, Chemical synthesis of a family of FBIs. The synthetic route starts from pyridines (or pyrimidines) and **1a**–**1c**, 4-bromoacetophenone **2**, to form adducts **3a**–**3c**. Coupling of these latter intermediates with aza-crown ethers **4a-c** yields compounds **5a**–**5c**, which reacts with 1,2-dibromoarenes **6a,b** to give the FIB candidates **7aa**–**7cb**. Numbers in parentheses correspond to the chemical yields (average values after three or five independent experiments) of isolated pure products. DavePhos, 2'-(dicyclohexylphosphino)-*N,N*-dimethyl-2-biphenylamine; dba, dibenzylideneacetone; XPhos, dicyclohexyl(2',4',6'-triisopropyl-2-biphenylyl) phosphine.

much faster decay rate. Near the end energy (Q), however, the $\beta\beta2\nu$ process is very strongly suppressed by kinematics, and its contamination to the $\beta\beta0\nu$ signal is very small for a detector with good energy resolution[18].

Instead, owing to the irreducible presence of trace amounts of the radioactive decays chains of [238]U and [232]Th in the materials of the detector, the corresponding false signatures need to be suppressed by a very large factor. The decays of other radioactive isotopes created by neutron activation are also a concern. All $\beta\beta$ experiments are built with ultrapure materials, operate in underground laboratories (to mitigate the impact of cosmic rays) and are protected by massive, ultrapure shields. These strategies reduce the ambient background by many orders of magnitude, but putative $\beta\beta0\nu$ events must still be extracted against tens of millions of spurious interactions.

The most powerful discriminant against backgrounds other than $\beta\beta2\nu$ would be the detection of the daughter atom, which is displaced

by two steps in the periodic table relative to its parent. In particular, the decay [136]Xe → [136]Ba^{2+} + 2e[−] + (2$\bar{\nu}_e$) will create a Ba^{2+} dication as the most likely outcome in xenon gas. In pure xenon gas, no known radioactive process will produce this ion in coincidence with two electrons. The implementation of a robust Ba^{2+} detection technique would facilitate the positive identification of a $\beta\beta0\nu$ candidate. The possibility of barium tagging in a xenon time-projection chamber (TPC) was proposed in 1991 by Moe[3] and has been extensively investigated for the past two decades[4,19,20].

Recently the nEXO collaboration demonstrated the imaging and counting of individual barium atoms in solid xenon by scanning a focused laser across a solid xenon matrix deposited on a sapphire window[5]. This is a promising step towards barium tagging in liquid xenon. The technique originally proposed by Moe and being pursued by nEXO relies on Ba^{+} fluorescence imaging using two atomic excitation levels in very-low-density gas. In liquid xenon, recombination is frequent
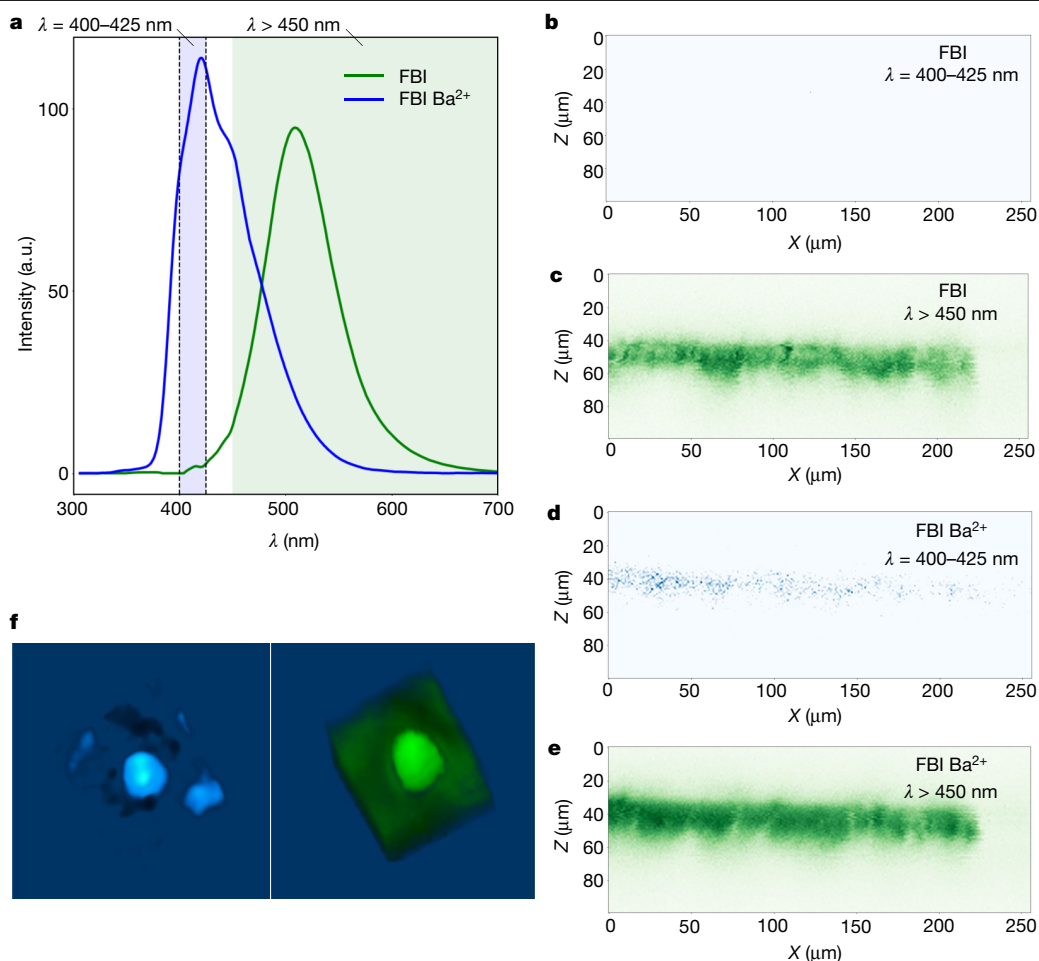
Fig. 2 | Response of the FBI. a, Emission spectrum of the SF (green line) and SBF (blue line) samples after silica subtraction (the SF spectrum is scaled by a factor of C_r with respect to the SBF spectrum). **b**, $Z–X$ profile of the control pellet, SFpA, showing no signal in the deep-blue region (400, 425) nm, where the contribution from unchelated molecules is negligible. **c**, $Z–X$ profile of SFpA in the green region ($\lambda > 450$ nm), showing intense green emission from the unchelated molecules. **d**, $Z–X$ profile of the sublimated pellet, SFpB, showing a clear signal in the deep-blue region (400, 425) nm due to the molecules chelated by the barium perchlorate. **e**, $Z–X$ profile of SFpB in the green region ($\lambda > 450$ nm), showing intense green emission from both chelated and unchelated molecules. **f**, 3D tomography images of SFpB, obtained with our TPA microscopy setup, passed through the blue and the green filters. The images reveal the shape of a tiny section (a square of 75 μm² size), showing the same landscape for both chelated and unchelated molecules.

and the barium daughters are distributed across charge states from 0 to 2+ (ref. [21]), with sizeable populations of neutral Ba and Ba⁺. In the high-pressure gas phase, however, the initially highly ionized barium daughter quickly captures electrons from neutral xenon, stopping at Ba²⁺, beyond which recombination is minimal[22].

A molecule with a response to optical stimulation that changes when it forms a supramolecular complex with a specific ion is a fluorescent indicator, and ions thus non-covalently bound to molecules are generally referred to as being chelated. In 2015, Nygren proposed a Ba²⁺ sensor based on fluorescent molecular indicators that could be incorporated within a high-pressure gas xenon TPC (HPXe)[6], such as those being developed by the NEXT Collaboration[17,23–25]. The concept was further developed in ref. [7] and was followed by an initial proof-of-concept study[8], which resolved individual Ba²⁺ ions on a thin quartz plate with Fluo-3 (a common indicator in biochemistry) suspended in polyvinyl alcohol (PVA) to immobilize the molecular complex and facilitate optical imaging. The experiment demonstrated single-ion sensitivity (with a root-mean-square super-resolution of 2 nm), which was confirmed by single-step photobleaching, and provided an essential step towards barium tagging in an HPXe.

However, an experiment aiming to detect Ba²⁺ in an HPXe requires a sensor that differs substantially from that used in ref. [8]. First, the surface density of indicators in the sensor needs to be high to ensure maximum ion capture efficiency. Second, the indicators must be able to form a supramolecular complex with Ba²⁺ in a dry medium, that is, the Gibbs energy of the process in xenon gas must be negative. Third, the indicators must respond to optical stimulation with a very distinctive signal that allows unambiguous identification of the molecule that has chelated the single ion produced in the $\beta\beta0\nu$ decay and good discrimination from the background due to the uncomplexed molecules in the surroundings. In other words, the discrimination factor, F, between the response (in a dry medium) of the chelated indicator and the residual response of unchelated molecules must be large. A considerable step in developing dry sensors was carried out in ref. [26], where molecular compounds based on aza-crown ethers and using fluorophores such as pyrene[27,28] and anthracene[29] were studied.

In this paper we demonstrate an important step towards a barium-tagging experiment in an HPXe, using a fluorescent bicolour indicator (FBI) as the core of a sensor that detects single Ba²⁺ ions in a high-pressure gas detector. The indicator is designed to bind strongly to Ba²⁺ and to shine very brightly when complexed with Ba²⁺. Furthermore, the emission spectrum of the chelated indicator is considerably blue-shifted with respect to the unchelated species, allowing an additional discrimination of almost two orders of magnitude.

Article
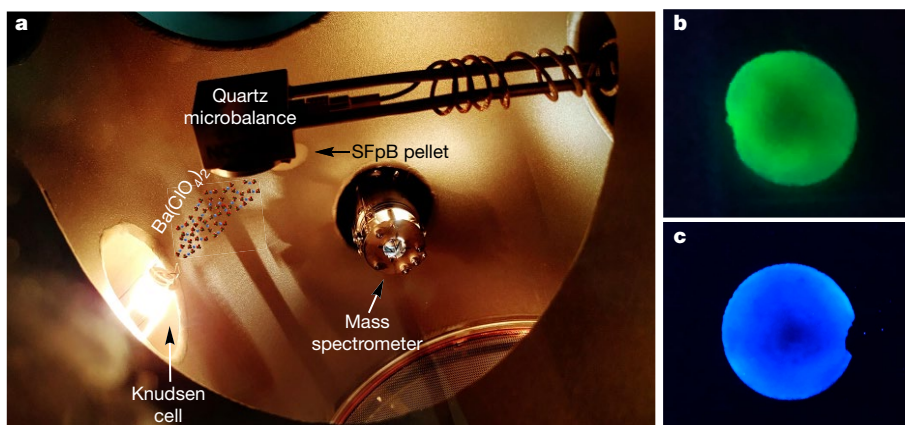
Fig. 3 | Sublimation of Ba(ClO₄)₂ on the FBI. a, Experimental setup. Photograph of the interior of the UHV chamber used for sublimation. The positions of the pellet, evaporator, quartz microbalance and mass spectrometer are indicated. **b**, **c**, Photographs of the pellet before (**b**) and after (**c**) the sublimation. In both cases, the excitation light is 365 nm. We note the characteristic green colour of unchelated FBI before the sublimation and the blue shift after the sublimation, which shows a large density of chelated molecules.

Design and synthesis of FBI compounds

Our criteria for designing FBIs are summarized in Fig. 1. The indicator includes, as essential components, a metal-binding group (a convenient moiety is a coronand formed by an *N*-aryl-aza-crown ether[30,31]) and a fluorophore, in line with previously developed designs for fluorescent sensors able to capture metal cations in solution[32]. Figure 1a shows the expected behaviour of a fluorescent monocolour indicator, in which the fluorophore does not modify substantially its π-molecular orbital structure upon metal coordination. In these hydrocarbon or heterocyclic scaffolds, an electron-donating group close to the fluorophore (for instance, an amino group of the aza-crown ether) can promote a photoinduced electron transfer that quenches the fluorescence in the absence of a binding cation. By contrast, sensor–cation complexation results in an off–on enhancement of the photoemission intensity[33] with $\Delta\lambda \approx 0$ (Fig. 1a). Therefore, in general only changes in the intensity of the emitted fluorescent signal upon Ba²⁺ complexation should be observed under this photoinduced electron transfer mechanism. This kind of sensor has been used in aqueous solution for metals of biological interest[34] and mainly for the capture of cations such as K⁺ by using bicyclic aza-cryptands[35]. Figure 1b illustrates the desired behaviour of an FBI indicator upon binding to Ba²⁺ ions. A convenient way to generate this kind of sensor with $\Delta\lambda \neq 0$ consists of generating an intramolecular photoinduced charge transfer (PCT) by modifying the interaction of an electron-donating group with the rest of the fluorophore[32]. Upon coordination with the cation, the change in the dipole moment of the supramolecular entity can generate a Stokes shift. However, in general these PCT phenomena promote only slight blue shifts[36] and depend on the polarity of the environment, thus being strongly affected by solvent effects. Actually, most PCT sensors work in water and bind cations such as Na⁺ and K⁺ by means of bicyclic aza-cryptands[37,38], among other groups such as acidic chelators or podands. Therefore, the design and chemical synthesis of efficient FBIs with large enough $\Delta\lambda$ values in the gas phase still constitutes an important challenge.

Within this context, we require that: (i) the chelating group binds the cation with a high binding constant; (ii) the indicator response in a dry medium is preserved and preferably enhanced with respect to the response in solution; and (iii) the fluorophore exhibits a distinct response in the visible region for the chelated and unchelated states (thus the term 'bicolour indicator'). To that end, the synthesis of FBI compounds incorporates a custom-designed fluorophore possessing two aromatic components, denoted as Ar¹ and Ar² in Fig. 1b that are connected by a free-rotating σ bond. The main fluorophore component Ar¹ consists of a nitrogen-containing aromatic polyheterocycle[39–42] that

can bind the Ba²⁺ cation, thus modifying its electronic structure and decoupling this moiety from Ar², which in turn can generate a π–cation interaction[43] (Fig. 1b). The expected shift in response to the coordination should provide a strong signature of a bound indicator, exhibiting a blue shift over a background of unbound species. Furthermore, we require that the indicator response does not form supramolecular complexes with light elements in the barium column of alkaline earth elements (such as beryllium, calcium and magnesium) as well as with other close alkali ions that are frequently found in the environment, such as Na⁺ and K⁺.

The chemical synthesis of our sensors is shown in Fig. 1c. The process starts with the double addition–elimination reaction between 2-aminopyridines (X = CH) **1a**,**c** or 2-aminopyrimidine **1b** (X = N) and 2,4-dibromoacetophenone **2**. Bicyclic heterocycles **3a**–**3c** react with aza-crown ethers **4a**–**c** in the presence of a Pd(0)/DavePhos catalytic system to generate intermediates **5a**–**5e** in moderate (30%) to very good (95%) yields. Finally, these latter adducts are coupled with aromatic 1,2-dibromides **6a**,**b** by means of a catalytic system formed by a Pd(II) salt and XPhos to yield the desired FBI compounds **7aa**–**7cb**. In this latter step, the formal (8 + 2) reactions are carried out in the presence of potassium carbonate or caesium carbonate (compound **7ec**) as weak bases.

Finally, we performed experiments to determine the photo-physical properties of compounds **7**. The results of these experiments, which are described in Methods, allowed us to select compound **7ca** as the optimal combination of structural and electronic features that fulfil our design criteria. We refer henceforth to compound **7ca** as FBI.

Discrimination factor

To demonstrate the performance of our FBI as a Ba²⁺ sensor, we adopted silica gel as a solid-phase support. Adsorption of the molecule on the silica surface permits the exposure of at least one side of its crown ether moiety to the interaction with Ba²⁺ cations. In addition, this solid–gas interface topology preserves the conformational freedom required to reach the coordination pattern observed in our calculations (see Methods for further information), keeping the essential features of our design, in particular the Ba²⁺-induced colour shift.

Two samples were manufactured. Sample SF was prepared by depositing on a silica pellet 2.3×10^{-5} mmol of FBI (from a CH₃CN solution) per milligram of silica. Sample SBF was formed by depositing 7.4×10^{-8} mmol of FBI (from a CH₃CN solution) per milligram of silica on a silica pellet saturated with barium perchlorate. The optimal concentration of barium salt was determined by a titration experiment
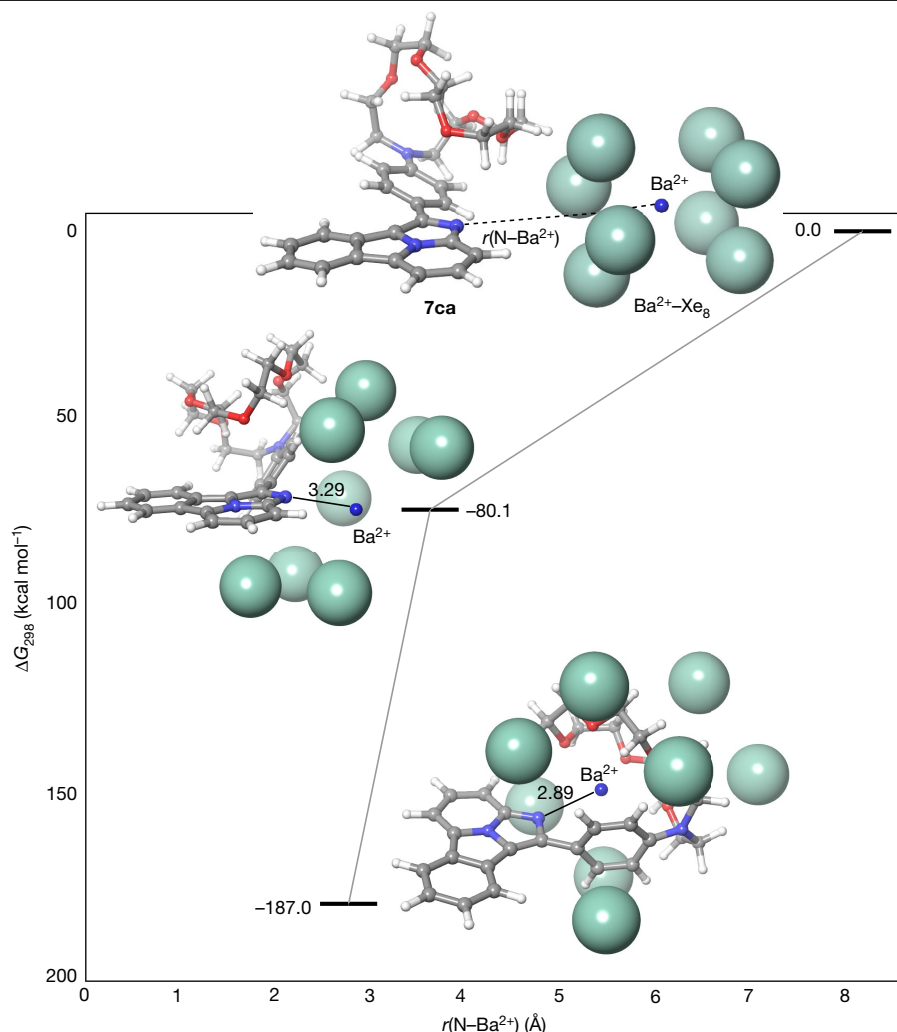
Fig. 4 | Computed structures of FBI (7ca) and a $Ba^{2+}Xe_8$ cluster at different N–Ba^{2+} distances. The geometries and energies shown were computed using DFT (see Methods for further details). Xenon atoms are represented using the Corey–Pauling–Koltun (CPK) space-filling model. The remaining atoms are represented using a ball-and-stick model and the CPK colouring code. Relative free energies (ΔG_{298}), have been computed at 25 °C (298 K).

described in Methods. The ratio between the FBI concentrations of SF and SBF was $C_r = 310 \pm 6$, where the 2% relative error was determined by propagating the uncertainties in the measurements of the volumes of the solutions. Figure 2a shows the emission spectra of the SF (SBF) samples for an excitation light of 250 nm, recorded by a fluorimeter after evaporating the solvent and subtracting the background signal due to the silica (see Methods for a discussion).

A robust separation between SF and SBF can be achieved by selecting a blue-shifted wavelength range of $\lambda_f = (\lambda_{min}, \lambda_{max})$ using a band filter. We call $C(\lambda)$ the emission spectrum of the chelated molecules (for example, the blue curve in Fig. 2a) and $U(\lambda)$ that of the unchelated molecules (green curve in Fig. 2a). The fraction of $C(\lambda)$ selected by the filter $f_c = c'/C$, where $c' = \int_{\lambda_{min}}^{\lambda_{max}} C(\lambda)\,d\lambda$ and $C = \int C(\lambda)\,d\lambda$. Analogously, the fraction of $U(\lambda)$ selected by the filter is $f_u = u/U$ with $u = \int_{\lambda_{min}}^{\lambda_{max}} U(\lambda)\,d\lambda$ and $U = \int U(\lambda)\,d\lambda$. By defining $D_r = f_c/f_u$, the discrimination factor is simply:

$$F = D_r C. \tag{1}$$

For this study we chose a band filter with $\lambda_f = (400, 425)$ nm, corresponding to the region shaded in blue in Fig. 2a. A larger separation could be obtained by including smaller wavelengths (for example, selecting $\lambda_f < 400$ nm), but the fluctuations associated with the subtraction of the baseline and the rapid variation of $C(\lambda)$ would also result in

large uncertainties. We find $f_c = 0.29 \pm 0.03$, $f_u = 0.0036 \pm 0.0007$ and $D_r = 80 \pm 18$ (all uncertainties denote the root-mean-square deviation). The approximately 20% relative error in the estimation of f_u is dominated by the subtraction of the baseline, whereas the approximately 10% relative error in the estimation of f_c is found by varying the range of the filter by ±1 nm. Using equation (1) we find

$$F = (25 \pm 6) \times 10^3. \tag{2}$$

A proof-of-concept study of chelation in a dry medium

An important step towards the detection of Ba^{2+} in an HPXe is the demonstration that the ions can be chelated in the absence of a solvent. This requires exposing a sample of FBI molecules deposited in a solid–vacuum interface to a source of Ba^{2+} ions.

To achieve this goal, we designed a sublimation experiment as follows. We started by compressing silica powder to form thin silica pellets, then we deposited a FBI–CH_3CN solution on the pellets and evaporated the solvent. Two similar SFp pellets (SFpA and SFpB) were prepared by depositing 7.4×10^{-8} mmol of indicator per milligram of silica, which is equivalent to 1.3×10^{15} molecules of FBI. SFpA was kept as a reference for unchelated molecules, and SFpB was introduced in an ultrahigh-vacuum chamber (Fig. 3a) in which barium perchlorate was sublimated. Sublimation was performed using a Knudsen cell at a

temperature of around 700 K. The evaporation rate was continuously monitored in situ with a microbalance. The total thickness of deposited $Ba(ClO_4)_2$ was 10 Å, equivalent to a layer of 7.6×10^{14} molecules. Figure 3b, c shows images of the pellet before and after sublimation under an excitation light of 365 nm. The blue shift after sublimation is clearly visible even to the naked eye, showing that a large number of indicators on the pellet's surface were chelated.

The next step was to scan both the SFpA and SFpB pellets in our two-photon absorption (TPA) microscopy setup[44], which is described in some detail in Methods. We performed tomography (for example, $Z–X$ scans) using two filters: a high-pass 'green' filter with $\lambda > 450$ nm and a band-pass 'deep blue' filter with wavelength (400, 425) nm. The $Z–X$ scans were performed with infrared light (800 nm) at a nominal laser power of 100 mW. In addition, we obtained three-dimensional (3D) tomography images, which were assembled from 40 $X–Y$ scans of 75 µm × 75 µm. Each scan corresponded to a different depth Z, in steps of 10 µm. The resulting images were then combined in a 3D image using custom software[45].

Our results are summarized in Fig. 2. We started by measuring the control pellet, SFpA. The $Z–X$ tomography image acquired using the green filter (Fig. 2c) reveals a region of about 20 µm in depth that corresponds to the area of the pellet where FBI molecules were immobilized. Because these are unchelated molecules, they are visible with this filter but not with the deep-blue filter (Fig. 2b). By contrast, for SFpB the green profile (Fig. 2e) is similar to the one measured for SFpA, but the deep-blue tomography (Fig. 2d) shows a clear signal in the same 20-µm region around the pellet surface. This can be exclusively ascribed to the emission of chelated molecules, therefore demonstrating that the sublimation deposited the Ba^{2+} uniformly, resulting in a layer of chelated molecules. Finally, Fig. 2f shows green and deep-blue 3D tomography images confirming that the spatial distribution of the chelated molecules follows that of the unchelated indicators.

Density functional theory (DFT) calculations (described in detail in Methods) show that the Gibbs energy associated with binding of $Ba(ClO_4)_2$ to FBI is −80 kcal mol^{-1}, confirming that the process is very exergonic, which is expected given the experimental result described above and is fully compatible with the high binding constant found for this process.

Chelation of Ba^{2+} by FBI indicators in xenon gas

In an HPXe experiment, the Ba^{2+} created in the $\beta\beta0\nu$ decay will slowly drift to the cathode, picking up on its way neutral xenon atoms in a variety of solvation states, thus yielding $[BaXe_N]^{2+}$ states (with $N = 1$, 2...). At the large pressures that are typical in an HPXe (~20 bar), it has been estimated[46] that $N \approx 8$.

What is the relevance of the proof-of-concept study described here (which demonstrates the observation of the reaction $Ba(ClO_4)_2 + FBI$ in vacuo) for an HPXe experiment, which requires that the reaction $[BaXe_N]^{2+} + FBI$ occurs efficiently in high-pressure xenon? DFT can shed light on this question. Our calculations show that the interaction between a $Ba^{2+}–Xe_8$ cluster and FBI results in a very exergonic process with a calculated Gibbs reaction energy of −195.9 kcal mol^{-1}. This value is almost as large as the Gibbs energy associated with the interaction of a naked dication with the indicator (−197.5 kcal mol^{-1}) and much larger than the energy associated with binding of $Ba(ClO_4)_2$ with FBI (−80.0 kcal mol^{-1}). Furthermore, we find that the Gibbs energy of FBI + Ba^{2+} changes very little in the range 1–30 bar (see Extended Data Table 3).

Finally, our calculations suggest that a layer of indicators with a density of about 1 molecule per square nanometre will efficiently chelate Ba^{2+}. Figure 4 shows the computed structures of FBI and a $Ba^{2+}–Xe_8$ cluster at different $N–Ba^{2+}$ distances. When optimization of the (**7ca**, $Ba^{2+}–Xe_8$) pair was started at a $N–Ba^{2+}$ separation of 8 Å, the cluster spontaneously converged to a local minimum at which the original

Xe_8 structure was squeezed around the convex face of FBI, and the $N–Ba^{2+}$ distance was 3.27 Å. From this intermediate state, the whole cluster converged to the chelated species, in which the $N–Ba^{2+}$ distance was found to be 2.9 Å. This latter energy minimum was calculated to be about 107 kcal mol^{-1} more stable than the previous intermediate state. In addition, the geometric parameters of the minimum-energy cluster −in which the eight Xe atoms are distributed around FBI− are very similar to those found for the FBI Ba^{2+} and FBI $Ba(ClO_4)_2$ complexes.

Conclusions

We have synthesized an FBI that could be the basis of a barium-tagging sensor in a future HPXe experiment searching for $\beta\beta0\nu$ decays. Using silica as a physical support, we have shown that the FBI has a very large discrimination factor of $F = (25 \pm 6) \times 10^3$ in a dry medium (silica–air). Furthermore, the indicator efficiently chelates Ba^{2+} in a dry medium (silica–vacuum). This was proved by sublimating barium perchlorate ($Ba(ClO_4)_2$) on FBI molecules deposited on a silica pellet and interrogating the indicators using TPA microscopy. To our knowledge, this is the first time that the formation of a Ba^{2+} supramolecular complex in a dry medium is demonstrated.

In addition, we have performed DFT calculations that show that our experimental result is consistent with the exergonic nature of the binding of $Ba(ClO_4)_2$ to the FBI in vacuo and for high solvation states of Ba^{2+} in xenon at all relevant pressures. Importantly, the process evolves spontaneously when the system FBI Ba^{2+} starts at distances of around 1 nm. From these calculations, we can conclude that the formation of supramolecular complexes observed in vacuo implies that FBI indicators can chelate Ba^{2+} ions with high efficiency in an HPXe experiment. We further show in Methods that the large value of F found for the FBI allows the unambiguous identification−using TPA microscopy−of a single chelated indicator.

Online content

Any methods, additional references, Nature Research reporting summaries, source data, extended data, supplementary information, acknowledgements, peer review information; details of author contributions and competing interests; and statements of data and code availability are available at https://doi.org/10.1038/s41586-020-2431-5.

1. Majorana, E. Theory of the symmetry of electrons and positrons. *Nuovo Cim.* **14**, 171–184 (1937).
2. Gómez Cadenas, J. J., Martín-Albo, J., Mezzetto, M., Monrabal, F. & Sorel, M. The search for neutrinoless double beta decay. *Riv. Nuovo Cim.* **35**, 29–98 (2012).
3. Moe, M. K. New approach to the detection of neutrinoless double beta decay. *Phys. Rev. C* **44**, 931–934 (1991).
4. Danilov, M. et al. Detection of very small neutrino masses in double beta decay using laser tagging. *Phys. Lett. B* **480**, 12–18 (2000).
5. nEXO Collaboration. Imaging individual barium atoms in solid xenon for barium tagging in nEXO. *Nature* **569**, 203–207 (2019).
6. Nygren, D. R. Detecting the barium daughter in ^{136}Xe 0-$\nu\beta\beta$ decay using single-molecule fluorescence imaging techniques. *J. Phys. Conf. Ser.* **650**, 012002 (2015).
7. Jones, B. J. P., McDonald, A. D. & Nygren, D. R. Single molecule fluorescence imaging as a technique for barium tagging in neutrinoless double beta decay. *J. Inst.* **11**, P12011 (2016).
8. McDonald, A. D. et al. Demonstration of single barium ion sensitivity for neutrinoless double beta decay using single molecule fluorescence imaging. *Phys. Rev. Lett.* **120**, 132504 (2018).
9. Sakharov, A. D. Violation of CP invariance, C asymmetry, and baryon asymmetry of the universe. *Pis'ma Z. Eksp. Teor. Fiz.* **5**, 32–35 (1967).
10. Fukugita, M. & Yanagida, T. Baryogenesis without grand unification. *Phys. Lett. B* **174**, 45–47 (1986).
11. Gell-Mann, M., Ramond, P. & Slansky, R. Complex spinors and unified theories. In *Proc. of Supergravity Stony Brook Workshop* (eds Van Nieuwenhuizen, P. & Freedman D. Z.) 27–29 (1979).
12. Yanagida, T. Horizontal symmetry and masses of neutrinos. *Prog. Theor. Phys.* **64**, 1103–1105 (1980).
13. Mohapatra, R. N. & Senjanovic, G. Neutrino mass and spontaneous parity nonconservation. *Phys. Rev. Lett.* **44**, 912–915 (1980).

14. Gando, A. et al. Search for Majorana neutrinos near the inverted mass hierarchy region with KamLAND-Zen. *Phys. Rev. Lett.* **117**, 082503–082506 (2016).

15. GERDA Collaboration. Improved limit on neutrinoless double-β decay of ^{76}Ge from GERDA Phase II. *Phys. Rev. Lett.* **120**, 132503–132505 (2018).

16. Alduino, C. et al. First results from CUORE: a search for lepton number violation via $0\nu\beta\beta$ decay of ^{130}Te. *Phys. Rev. Lett.* **120**, 132501–132508 (2018).

17. Gomez-Cadenas, J. J. Status and prospects of the NEXT experiment for neutrinoless double beta decay searches. Preprint at https://arxiv.org/abs/1906.01743 (2019).

18. Elliott, S. R. & Vogel, P. Double beta decay. *Annu. Rev. Nucl. Part. Sci.* **52**, 115–151 (2002).

19. Sinclair, D. et al. Prospects for barium tagging in gaseous xenon. *J. Phys. Conf. Ser.* **309**, 012005 (2011).

20. Mong, B. et al. Spectroscopy of Ba and Ba$^+$ deposits in solid xenon for barium tagging in nEXO. *Phys. Rev. A* **91**, 022505–022513 (2015).

21. EXO-200 Collaboration. Measurements of the ion fraction and mobility of α- and β-decay products in liquid xenon using the EXO-200 detector. *Phys. Rev. C* **92**, 045504–045510 (2015).

22. Bolotnikov, A. & Ramsey, B. The spectroscopic properties of high-pressure xenon. *Nucl. Instrum. Methods Phys. Res. A* **396**, 360–370 (1997).

23. Nygren, D. High-pressure xenon gas electroluminescent TPC for 0-ν $\beta\beta$-decay search. *Nucl. Instrum. Methods Phys. Res. A* **603**, 337–348 (2009).

24. Álvarez, V. et al. NEXT-100 Technical Design Report (TDR). Executive summary. *J. Inst.* **7**, T06001 (2012).

25. Martín-Albo, J. et al. Sensitivity of NEXT-100 to neutrinoless double beta decay. *J. High Energy Phys.* **2016**, 159 (2016).

26. Thapa, P. et al. Barium chemosensors with dry-phase fluorescence for neutrinoless double beta decay. *Sci. Rep.* **9**, 15097 (2019).

27. Ji, H.-F., Dabestani, R., Brown, G. M. & Hettich, R. Spacer length effect on the photoinduced electron transfer fluorescent probe for alkali metal ions. *Photochem. Photobiol.* **69**, 513–516 (1999).

28. Nakahara, Y., Kida, T., Nakatsuji, Y. & Akashi, M. Fluorometric sensing of alkali metal and alkaline earth metal cations by novel photosensitive monoazacryptand derivatives in aqueous micellar solutions. *Org. Biomol. Chem.* **3**, 1787–1794 (2005).

29. Bissell, R. A. et al. Luminescence and charge transfer. Part 2. Aminomethyl anthracene derivatives as fluorescent pet (photoinduced electron transfer) sensors for protons. *J. Chem. Soc. Perkin Trans.* **2** 9, 1559–1564 (1992).

30. Bourson, J., Pouget, J. & Valeur, B. Ion-responsive fluorescent compounds 4 effect of cation binding on the photophysical properties of a coumarin linked to monoaza- and diaza-crown ethers. *J. Phys. Chem.* **97**, 4552–4557 (1993).

31. Li, J., Yim, D., Jang, W.-D. & Yoon, J. Recent progress in the design and applications of fluorescence probes containing crown ethers. *Chem. Soc. Rev.* **46**, 2437–2458 (2017).

32. Valeur, B. & Berberan-Santos, M. N. in *Molecular Fluorescence – Principles and Applications* 420–436 (Wiley–VCH, 2012).

33. Huston, M. E., Haider, K. W. & Czarnik, A. W. Chelation enhanced fluorescence in 9,10- bis[[(2-(dimethylamino)ethyl)methylamino]methyl]anthracene. *J. Am. Chem. Soc.* **110**, 4460–4462 (1988).

34. Carter, K. P., Young, A. M. & Palmer, A. E. Fluorescent sensors for measuring metal ions in living systems. *Chem. Rev.* **114**, 4564–4601 (2014).

35. Golchini, K. et al. Synthesis and characterization of a new fluorescent probe for measuring potassium. *Am. J. Physiol.* **258**, F438–F443 (1990).

36. Yang, J.-S., Hwang, C.-Y., Hsieh, C.-C & Chiou, S.-Y. Spectroscopic correlations between supermolecules and molecules. Anatomy of the ion-modulated electronic properties of the nitrogen donor in monoazacrown-derived intrinsic fluoroionophores. *J. Org. Chem.* **69**, 719–726 (2004).

37. Smith, G. A., Hesketh, J. C. & Metcalfe, T. R. Design and properties of a fluorescent indicator of intracellular free sodium concentration. *Biochem. J.* **250**, 227–232 (1988).

38. Crossley, R., Goolamali, Z. & Sammes, P. G. Synthesis and properties of a potential extracellular fluorescent probe for potassium. *J. Chem. Soc. Perkin Trans.* **2** 7, 1615–1623 (1994).

39. Aginagalde, M. et al. Tandem [8 + 2] cycloaddition-[2 + 6 + 2] dehydrogenation reactions involving imidazo[1,2-a]pyridines and imidazo[1,2-a]pyrimidines. *J. Org. Chem.* **75**, 2776–2784 (2010).

40. Zhang, Y., Tang, S., Thapaliya, E. R., Sansalone, L. & Raymo, F. M. Fluorescence activation with switchable oxazines. *Chem. Commun.* **54**, 8799–8809 (2018).

41. Ko, C.-C. & Yam, V. W.-W. Coordination compounds with photochromic ligands: ready tunability and visible light-sensitized photochromism. *Acc. Chem. Res.* **51**, 149–159 (2018).

42. Maitra, R., Chen, J.-H., Hu, C.-H. & Lee, H. M. Synthesis and optical properties of push-push- pull chromophores based on imidazo[5,1,2-cd]indolizines and naphtho[1',2':4,5]imidazo[1,2-a]pyridines. *Eur. J. Org. Chem.* 5975–5985 (2017).

43. Dougherty, D. A. The cation–π interaction. *Acc. Chem. Res.* **46**, 885–893 (2013).

44. Ávila, F. J., Gambín, A., Artal, P. & Bueno, J. M. In vivo two-photon microscopy of the human eye. *Sci. Rep.* **9**, 10121 (2019).

45. Bueno, J. et al. Multiphoton microscopy of ex vivo corneas after collagen cross-linking. *Invest. Ophthalmol. Vis. Sci.* **52**, 5325–5331 (2011).

46. Bainglass, E., Jones, B. J. P., Foss, F. W., Huda, M. N. & Nygren, D. R. Mobility and clustering of barium ions and dications in high pressure xenon gas. *Phys. Rev. A* **97**, 062509 (2018).

Article

Methods

Photophysics and supramolecular chemistry of FBI indicators in solution

Our experiments to determine the photophysical properties of compounds **7** started by recording their respective emission spectra in acetonitrile solution. Although all compounds were fluorescent with large intensities in the minimum-energy transitions, the critical criterion to select the most suitable candidate was the ability of a given compound to exhibit different lowest emission wavelengths in their unbound and barium-coordinated forms. We defined the peak discrimination factor f_λ at a given wavelength λ as:

$$f_\lambda = \frac{I_\lambda(7Ba^{2+}) - I_\lambda(7)}{I_\lambda(7)} \qquad (3)$$

where $I_\lambda(7Ba^{2+})$ and $I_\lambda(7)$ are the intensities of the emission signals at wavelength λ of the corresponding bound ($7Ba^{2+}$) and free (**7**) fluorophore. In addition, we measured the molecular brightness[34] B_λ of each transition according to the following expression:

$$B_\lambda = \varepsilon_\lambda \phi_\lambda \qquad (4)$$

where ε_λ is the molar extinction coefficient and ϕ_λ is the emission quantum yield.

The data associated with the photophysics of compounds **7** are listed in Extended Data Table 1. According to our results, compound **7aa**, which possesses the 1,4,7-trioxa-10-azacyclododecane moiety (**4a**, $n=1$), does not show any substantial difference between the free and barium-bound states, thus indicating that this four-heteroatom aza-crown ether is too small to accommodate the Ba^{2+} cation. Compound **7ba**, with a 1,4,7,10-tetraoxa-13-azacyclopentadecane unit (**4b**, $n=2$), showed a noticeable blue shift upon coordination with Ba^{2+} ($\Delta\lambda = -54$ nm). However, the low value of f_λ makes this size of the chelating group not optimal for further development. In the case of the FBI molecule **7ca**, which incorporates the six-heteroatom-containing aza-crown ether unit 1,4,7,10,13-pentaoxa-16-azacyclooctadecane (**4c**, $n=3$), a larger blue shift associated with Ba^{2+} coordination ($\Delta\lambda = -61$ nm) is observed. Most importantly, the f_λ discrimination factor is found to be of the order of 180, which shows a considerable separation between the unbound **7ca** and the Ba^{2+}-coordinated **7ca**Ba^{2+} species. Both emission spectra are displayed in Extended Data Fig. 1. In addition, both unbound and cationic species show acceptable quantum yields and molecular brightness values.

As far as the chemical structure of the tetracyclic fluorophore is concerned, our results indicate that introducing an additional nitrogen heteroatom in the 2,2a[1]-diazacyclopenta[jk]fluorene to form the corresponding 2,2a[1],3-triazacyclopenta[jk]fluorine analogue is detrimental in terms of quantum yield and molecular brightness, as concluded from the photophysical properties of compound **7da** shown in Extended Data Table 1. Moreover, the presence of an additional fused phenyl group in the fluorophore results in the formation of imidazo[5,1,2-cd]naphtho[2,3-a]indolizine derivative **7cb**, which has an f_λ factor considerably lower than that measured for **7ca**. Therefore, the presence of additional fused aromatic or heteroaromatic rings to the basic benzo[a]imidazo[5,1,2-cd]indolizine scaffold does not improve the photophysical properties of the resulting cycloadduct. Finally, the presence of an electron-withdrawing group in compound **7ec** results in a quenching of the quantum yield of the fluorophore, as well as a lowering of the discrimination factor. According to these results, further chemical elaboration of the fluorophore skeleton in order to synthesize the spacer and linker groups shown in Extended Data Fig. 1a must not involve carboxy derivatives such as esters or amides, but π-decoupled moieties such as alkoxy groups. Therefore, we conclude that **7ca** is the optimal combination of structural and electronic features to fulfil our previously defined design criteria.

Having selected compound **7ca** as the best FBI candidate, we conducted studies to assess its binding ability, which must be high (in a dry medium) for our sensor. To that end, we first measured its cation association constant K_a with barium perchlorate in acetonitrile at 298 K using the Benesi−Hildebrand method[47] and the corresponding fluorescence spectra, according to the following formula[48]:

$$\frac{1}{F - F_{\min}} = \frac{1}{F_{\max} - F_{\min}}\left(1 + \frac{1}{K_a[Ba^{2+}]}\right) \qquad (5)$$

In this expression, F is the measured emission of compound **7ca** at the excitation wavelength $\lambda_{\mathrm{exc}} = 250$ nm in the presence of a given $[Ba^{2+}]$ concentration, and $F_{\min}$ and $F_{\max}$ represent the corresponding intensities of the free aza-crown ether **7ca** and the host−guest complex **7ca**Ba^{2+}, respectively. Under these conditions and on the basis of the data shown in Extended Data Fig. 1d, we measured a binding constant of $K_a = 5.26 \times 10^4\,M^{-1}$ ($R^2 = 0.953$, where R^2 is the coefficient of determination). This indicates the good efficiency of compound **7ca** for Ba^{2+} capture and formation of the (**7ca**Ba^{2+})(ClO_4^-)$_2$ salt in solution; the favourable photophysical parameters of the compound are listed in Extended Data Table 1. In addition, the Job plot shows a maximum for $n = m = 1$, indicating that **7ca** captures only one Ba^{2+} cation per molecule, as shown in Extended Data Fig. 1e.

Electronic structure calculations and nuclear magnetic resonance experiments

Electronic structure calculations at the DFT level both in the gas phase and in solution confirm the strong binding affinity of **7ca** to coordinate Ba^{2+}. The optimized **7ca**Ba^{2+} structure exhibits a large molecular torsion of the binding group with respect to the free **7ca** molecule (see the dihedral angle ω in Extended Data Fig. 2b) so that a molecular cavity appears, with the metal cation forming a π-complex between the Ba^{2+} metallic centre and the phenyl group. The oxygen atoms of the aza-crown ether occupy five coordination positions with O−Ba contacts within the range of the sum of the van der Waals radii (2.8–3.0 Å)[49]. Interestingly, the phenyl ring attached to the crown ether is oriented towards the centre of the cavity coordinating Ba^{2+} through the π-electrons. The frontier molecular orbitals of **7ca** are delocalized over the entire fluorophore moiety, with virtually no participation of the binding-group electrons (Extended Data Fig. 2c). The lowest bright state of the unbound FBI molecule can be mainly characterized as the electronic transition between the highest occupied molecular orbitals (HOMO) and the lowest unoccupied molecular orbitals (LUMO). Molecular distortion upon metal coordination in **7ca**Ba^{2+} has an important impact on the electronic structure. In particular, the torsion of the phenyl group allowing π-coordination breaks the planarity with the rest of the fluorophore, modifying the HOMO and LUMO energy levels. The decrease of the effective conjugation with respect to **7ca** increases the symmetry allowed $\pi \rightarrow \pi^*$ gap, thus resulting in the blue shift of the fluorescent emission (Extended Data Fig. 2c). Therefore, these results support the viability of **7ca** as an efficient Ba^{2+} indicator in both wet and dry conditions (see Supplementary Information).

Nuclear magnetic resonance (NMR) experiments on the complexation reaction between the FBI molecule **7ca** and barium perchlorate are compatible with the geometries obtained by the DFT calculations. Progressive addition of the salt promoted a deshielding to lower field of the protons of the para-phenylene group marked as b in Extended Data Fig. 2d, which are in ortho disposition with respect to the aza-crown ether. The meta protons marked as c in Extended Data Fig. 2d showed a similar, but lower in magnitude, deshielding effect. The remaining protons of the benzo[a]imidazo[5,1,2-cd]indolizine fluorophore showed a very light deshielding effect but remained essentially unchanged. Instead, the 1,4,7,10,13-pentaoxa-16-azacyclooctadecaane moiety of

7ca showed different deshielding effects upon coordination with Ba^{2+}, with the only exception being the *N*-methylene protons denoted as *a* in Extended Data Fig. 2e, which were shifted to a higher field, thus demonstrating that the nitrogen atom of the aza-crown ether does not participate in the coordination with the dication.

Computed structures of free and complexed FBI

The optimized molecular geometry of the adduct between FBI (**7ca**) and $Ba(ClO_4)_2$ (Extended Data Fig. 3) at the DFT level of theory shows a compact structure in which the Ba^{2+} centre does not interact only with the full aza-crown ether but extends its coordination pattern to the N1 atom of the benzo[*a*]imidazo[5,1,2-*cd*]indolizine aromatic tetracycle and to the 1,4-disubstituted phenyl group. Consequently, the nitrogen atom N2 of the aza-crown ether is shifted away from the closest coordination sphere of Ba^{2+} (compare the Ba^{2+}–N1 and Ba^{2+}–N2 distances in Extended Data Table 2). The two perchlorate anions interact with the metallic centre by blocking the extremes of the channel formed by **7ca**, with the Ba^{2+}–O distances only about 0.1 Å larger than those computed for $Ba(ClO_4)_2$. This geometry of **7ca**$Ba(ClO_4)_2$ results in decoupling between the two components of the fluorophore, with $\omega = 45°$. The calculated Gibbs energy associated with the binding of $Ba(ClO_4)_2$ with the FBI is −80 kcal mol^{-1}. This exergonic character is fully compatible with the high binding constant found for this process.

DFT calculations including a naked Ba^{2+} cation bound to **7ca** also showed a rigid structure, in which the main features observed for the **7ca**$Ba(ClO_4)_2$ complex −namely, the interaction of the metallic centre with the N1 atom, the oxygen atoms of the aza-crown ethers and the 1,4-disubstituted aromatic ring−are even more pronounced (Extended Data Table 2 and Extended Data Fig. 3). In addition, the reaction is much more exergonic (Gibbs energy of the reaction, $\Delta G_{rxn} = -197.5$ kcal mol^{-1}; see Extended Data Table 3). The computed energies exhibit a very small dependence on pressure.

If the formation of clusters between the barium cation and the xenon atoms is considered, the interaction of a Ba^{2+}–Xe_8 cluster −a species that can be operative under high-pressure conditions−with the FBI results in a still very exergonic process, with a Gibbs reaction energy of −195.9 kcal mol^{-1}. All these results indicate that the findings obtained in solution for the interaction of the FBI compound and barium perchlorate are closely related to the features of the same process in the gas phase involving naked (or Xe-clusterized) barium dications.

Polymer and titration experiments

To measure the response of the FBI in dry media, we studied several materials, including silica (which we selected as our preferred support) and three different polymers: polyvinyl alcohol (PVA), poly(methyl metacrylate) (PMMA) and poly(ether blockamide) (PEBAX 2533).

In the case of silica we conducted a titration experiment, adding increasing concentrations of $Ba(ClO_4)_2$ to the gel before depositing the FBI–acetonitrile solution (in each case measurements were performed in a fluorimeter after drying the solvent). Our results are shown in Extended Data Fig. 4a. We found that the response of the complexed FBI indicator improved with larger concentrations of $Ba(ClO_4)_2$−an effect that we attribute to the affinity of the silica for barium. For the calculation of *F* we chose the largest concentration studied (7,927 equiv.).

We note, however, that the discrimination factor computed with a concentration of 3,964 equiv. (and with concentrations larger than 7,927 equiv., not shown in the plot) yields a very similar result, compatible with the error quoted for *F*. Our results for the studies with polymers are summarized in Extended Data Fig. 4b, which shows the response of the indicator in PMMA. Under an excitation light of 350 nm, the spectra of both chelated and unchelated molecules are similar and cannot be effectively separated. All the other polymers exhibit a similar behaviour. We attribute the lack of separation between the spectra of chelated and unchelated indicators to the restriction of the conformational freedom imposed by the polymer's rigid environment.

Subtraction of the silica response

Extended Data Figure 5 shows the response of the silica to an excitation light of 250 nm. We note that the subtraction of the silica response results in a zero baseline (and a significant subtraction error) for wavelengths below ~370 nm. Above that value, the chelated spectrum rises quickly, while the unchelated spectrum increases only above ~400 nm. The separation between the two spectra is very large in the region (400, 425) nm, where the response of the uncomplexed spectrum is compatible with zero, but the systematic error in the measurement of the discrimination factor is also large (40%). In the selected region of (400, 425) nm, the separation is still large and the systematic error is reduced to 20%.

Laser setup

A schematic diagram of our laser setup is depicted in Extended Data Fig. 6a. We took advantage of the fact that the emission spectra of the FBI and FBI Ba^{2+} for an excitation light of 250 nm and of 400 nm are very similar (Extended Data Fig. 6b) and used a mode-locked Ti:sapphire infrared laser (800 nm) as the illumination source, inducing the absorption of two photons of 400 nm each. This laser system provided pulses of infrared light with a repetition rate of 76 MHz. The pulse duration was 400 fs on the sample plane. The beam was reflected on a dichroic mirror, passed a non-immersion objective (20×, NA = 0.5) and reached the sample, illuminating a spot limited by diffraction to a volume of about 1 μm^3. A d.c. motor coupled to the objective allowed optical sectioning across the sample along the *Z* direction. This image modality is known as *Z*–*X* tomographic imaging and we call these tomographic images 'profiles'. In addition, we obtained 3D tomography images, which were assembled from 40 *X*–*Y* scans of 75 μm × 75 μm. Each scan corresponded to a different depth *Z*, in steps of 10 μm. The resulting images were then combined in a 3D image. The emitted light was collected through the same objective and passed the dichroic mirror. Finally, before reaching the photomultiplier tube used as the detection unit, the TPA signal passed through either a high-pass, green filter with $\lambda > 450$ nm, or a band-pass deep-blue filter of (400, 425) nm.

To estimate the absolute number of fluorescence photons emitted by the FBI indicator in a TPA scan, we first measured a reference sample of fluorescein suspended in PVA (fluorescein reference sample, FRS). Extended Data Fig. 6c shows a log–log plot of the recorded photomultiplier tube (PMT) signal as a function of the laser power for FRS. As expected for TPA, the slope of the resulting straight line has a value near 2. Extended Data Fig. 6d shows a profile taken on FRS at a power of 80 mW. Identical profiles were taken on SBFp at a power of 40 mW. This allowed the measurement of the brightness ratio $\delta_r = \delta_{SBFp}/\delta_{FRS}$, which gave $\delta_r = 17 \pm 4$ and therefore $\delta_{FBIBa^{2+}} = (6.2 \pm 1.7) \times 10^2$ GM (in units of Goeppert Mayer; 1 GM = 10^{-50} cm^4 s per photon per molecule). The details of the measurement are discussed below.

Determination of the brightness of FBI relative to fluorescein

The fluorophore brightness ($\delta = \sigma\phi_\lambda$, where σ is the TPA cross-section and ϕ_λ is the quantum yield) of fluorescein at a wavelength of 800 nm (ref. [50]) is $\delta_{fluo} = 36 \pm 9.7$ GM. It is therefore possible to normalize the brightness of the FBI to that of fluorescein by using samples of known concentrations and measuring the response in our setup for identical profiles. To that end, we used a control sample of fluorescein suspended in PVA (FPVA) with a concentration of $n_{FPVA} = 10^{13}$ molecules cm^{-3} and compared it with an FBI-chelated pellet (SBFp), which had a concentration of $n_{SBFp} = 2.2 \times 10^{17}$ molecules cm^{-3}. Profiles were taken on FPVA at a power of 500 mW. Identical profiles were taken on SBFp at a power of 100 mW. The total integrated PMT signal in the FPVA and SBFp samples is:

$$I = Kn\delta P^2 \tag{6}$$

Article

where n is the density of molecules (molecules cm^{-3}) of the sample and P is the laser power. K is a constant that depends on the setup, which is the same for the FPVA and SBFp profiles. It follows that:

$$R_{FBI/fluo} = \frac{\delta_{SBFp}}{\delta_{FPVA}} = \frac{I_{SBFp}}{I_{FPVA}} \frac{n_{FPVA}}{n_{SBFp}} \left(\frac{P_{FPVA}}{P_{SBFp}}\right)^2 \qquad (7)$$

All the quantities in equation (7) are known. In particular, the integral of the SBFp profile yields 10^9 PMT counts, whereas the integral of the FPVA profile has 5.9×10^4 counts. Thus, we find $R_{FBI/fluo} = 17 \pm 4$, where the ~20% relative error is dominated by the uncertainty in the concentration n_{SBFp}, and therefore $\delta_{FBIBa^{2+}} = (6.2 \pm 1.7) \times 10^2$ GM.

Interaction of FBI with other elements

The interaction of the FBI (**7ca**) with other elements was studied in order to assess the selectivity of the indicator. In particular, we chose several dications within the alkaline earth elements, one of which is barium, as well as sodium and potassium, which are abundant in the environment and occupy contiguous positions in the alkaline group of the periodic table. We prepared solutions (5×10^{-5} M) of **7ca** and a metal source in a ratio of 1:1. We used $Ca(OH)_2$, $K(ClO_4)$, $Na(ClO_4)$, $Mg(ClO_4)_2$, $Sr(ClO_4)_2$ and $Ba(ClO_4)_2$ with CH_3CN as the solvent. The results are summarized in Extended Data Fig. 7. We observed that Mg^{2+} induced a partial intensity lowering (on–off effect) at the same emission wavelength upon interaction with **7ca**, whereas Ca^{2+} did not produce any noticeable change in its fluorescence emission spectrum when mixed with **7ca**. Therefore, we concluded that our indicator does not produce substantial changes to the emission wavelength in the presence of light alkaline earth dications. By contrast, in the presence of **7ca**, Sr^{2+} exhibited an emission spectrum similar to that observed for Ba^{2+}. These results show that **7ca** is able to chelate the heavier alkaline earth dications Sr^{2+} and Ba^{2+}. It is therefore expected that **7ca** should chelate Ra^{2+}. Finally, according to our results, neither K^+ nor Na^+ were chelated by **7ca**, thus evidencing the high selectivity of our indicator.

A sensor for Ba^{2+} tagging

In addition to a sensor capable of chelating Ba^{2+} with high efficiency, a future HPXe experiment with barium tagging needs to be able to distinguish unambiguously the signal of a single complexed indicator from the background of unchelated surrounding molecules. Here we show that the large discrimination factor of the FBI permits such a robust observation of single chelated molecules even for densely packed sensors.

We consider a TPA microscopy system similar to the one used here, but with optimized parameters, for example, an 800-nm pulsed laser, with a repetition rate of $f = 100$ MHz, pulse width $\tau = 100$ fs full-width at half-maximum and a moderately large numerical aperture of NA = 0.95. Following ref. [51], we take the overall light collection efficiency of the system to be $\varepsilon_c = 10\%$. Focusing the laser on a diffraction-limited spot (a circle of ~0.5 μm diameter) results in a photon density of 1.7×10^{31} photons cm^{-2} W^{-2} per pulse.

We assume now that a single FBI molecule complexed with a Ba^{2+} ion and m unchelated indicators are contained in such a diffraction-limited spot. The number of absorbed photons, n_a, per fluorophore and per pulse is[52]:

$$n_a = \frac{P^2 \delta}{\tau f} \left(\frac{NA^2}{2\hbar c \lambda}\right)^2 \qquad (8)$$

where P is the laser power, δ is the brightness ($\sigma\phi_\lambda$) of the fluorophore, $\hbar$ is the reduced Planck constant and c is the speed of light in vacuum. We can compute the number of photons that the chelated indicator absorbs as a function of the laser power using equation (8). Given the relatively large TPA cross-section of the FBI (also computed here), $n_a = 2$ for a modest power of 11 mW. By setting the laser power at this

value, the emission rate of the chelated molecule will equal the laser repetition rate, $n_f = 1 \times 10^8$ photons s^{-1}.

The light emitted by the complexed FBI molecule will be blue-shifted. We assume that a band filter λ_f of (400, 425) nm is placed in front of the CCD. n_f is the fluorescence emitted in a given time interval by the chelated indicator. Then, the light recorded by the CCD that is due to the chelated indicator will be $N = \varepsilon_f \varepsilon_c n_f$, where $\varepsilon_f \approx 0.29$ is the band-pass filter efficiency for the signal.

The total fluorescence (green-shifted) emitted by the unchelated molecules will be mn_f/C, and the corresponding background light recorded by the CCD will be $N_b = \varepsilon_f' \varepsilon_c mn_f/C$, where $\varepsilon_f' \approx 0.0036$ is the band-pass filter efficiency for the background.

The total signal N_t recorded in the CCD will be $N_t = N_f + N_b$, where N_f is the fluorescent signal. The estimator of the signal observed in the spot will be $N_t - N_b$, where N_b can be computed with great precision by taking the average of a large number of spots containing only unchelated molecules. The signal-to-noise ratio (SNR) of the subtraction is:

$$SNR = \frac{N_f}{\sqrt{N_b}} = \sqrt{\varepsilon_f \varepsilon_c \frac{n_f F}{m}} = \sqrt{\frac{7.2 \times 10^{10}}{m}} \qquad (9)$$

in units of s$^{1/2}$. The SNR is expressed as a function of time in seconds because n_f measures the number of photons per second. The number of molecules in the diffraction spot will depend on the density of indicators, ρ, in the sensor. We assume that the target will be a dense monolayer with about one molecule per square nanometre. As shown by our DFT calculations, the 'snowballs' formed by the barium ion during transport (for example, $Ba^{2+}Xe_8$) will readily form a supra-molecular complex at distances of the order of 1 nm (for example, 8 Å in the example discussed here). Thus, $\rho = 10^6$ μm^{-2} and $m = 2 \times 10^5$. By substituting in equation (9), we find SNR $= 6 \times 10^2$ s$^{1/2}$. If we take a scanning time per spot of 1 ms, then SNR ≈ 20. Therefore, a chelated indicator would produce an unmistakable signal above the background of unchelated molecules in that spot. This demonstrates that fast and unambiguous identification of Ba^{2+} ions in the sensor can be attained using a dense monolayer. The scanning of large surfaces using wide-field TPA is discussed below.

A BOLD concept

We conceive the Barium atOm Light Detector (BOLD), which is an HPXe implementing a full barium-tagging detector (BTD) that fully covers the cathode of the apparatus. Other possibilities that could apply to a future HPXe with barium tagging are discussed in ref. [53].

BOLD consists of three major systems. An energy-tracking detector (ETD), which measures the energy and the start time t_0 of the event and reconstructs its topology (and in particular its barycentre), and the BTD, which is capable of tagging, with high efficiency, the single Ba^{2+} ion produced in a $\beta\beta0\nu$ or $\beta\beta2\nu$ decay. The information of these two systems is linked through the delayed coincidence trigger (DCT), which establishes a coincidence between the observation of the two-electron signal and the detection of Ba^{2+}. The role of the DCT is to suppress the impact of $\beta\beta2\nu$ events and of other potential accidental coincidences involving ions such as Ra^{2+} and Sr^{2+}.

Extended Data Fig. 8 shows a schematic of BOLD. Conceptually, the detector is as follows: the ETD is an array of light sensors (probably silicon PMTs) located behind the transparent anode, which is connected to high voltage. The BTD is located behind the grounded cathode and deploys an array of tiles called Molecular Target Elements (MTEs). A self-assembled monolayer of FBI indicators is grown on one of the sides of the MTEs, and placed facing the TPC fiducial volume. The MTEs are interrogated by a fast TPA laser microscopy system (TPAL) consisting of one or more pressure-resistant objectives, which are able to move on demand to the specific area of the BTD that needs to be scanned. The laser will be a high-power (2–3 MW), pulsed, femtosecond, 100-MHz (or 1-GHz) system that enters the chamber through suitable windows and is steered by piezo-electric actuated mirrors.

A prototype of such a system is already under development as a part of the NEXT R&D programme[53].

The delayed coincidence trigger is activated by the ETD when the energy of the event is measured to be within the region of interest, signalling an event of interest. When this happens, the ETD reconstructs the barycentre of the event and computes the expected time of arrival of the Ba^{2+} ion to the BTD. It then sends the coincidence trigger, which lowers the voltage of the BTD during a time window large enough (about 1 ms) to allow the putative Ba^{2+} ion arriving to the cathode to 'cross the gate', reach the BTD and be captured by one of the MTEs. The predicted arrival position of the ion is also known from the barycentre of the event (with a resolution of about 5 mm at a pressure of 40 bar, according to our Monte Carlo calculations) and is sent to the TPAL, which scans a region around it. After scanning, the TPAL sends a signal if a chelated molecule has been found. The signature of a $\beta\beta0\nu$ event is the coincidence between the energy trigger, the time trigger opening the cathode gate, and the TPAL positive trigger.

Given the barycentre resolution of 5 mm, the Ba^{2+} candidate will be contained in a scanning region of 1.5 cm × 1.5 cm more than 99% of the times. To scan such an area in a reasonable time, it is necessary to implement large-field-of-view (FOV) techniques. For example, a FOV of 100 μm diameter and an interrogation rate of 1 ms per FOV result in a scanning time of 13 s cm^{-2}, which allows the scanning of the barium fiducial area (1.5 cm × 1.5 cm) in ~30 s.

Indeed, the availability of lasers with peak powers of several watts makes fast scanning possible by using wide-field two-photon microscopy[54]. If, instead of focusing into a diffraction-limited spot by overfilling the back aperture of the objective (as discussed in the example given in the main text), we choose to focus into a small spot near the back aperture, a wider (and weaker) spot is produced on the target plane. The number of absorbed photons in this configuration decreases with $(r/r_d)^2$, where r is the wide-field radius and r_d is the radius of the diffraction limit spot. By taking $r = 50$ μm and $r_d = 0.5$ μm, we find that $n_a^{wf} = n_a \times 10^{-4}$, where n_a^{wf} is the number of absorbed photons in the wide-field configuration. However, these four orders of magnitude can be accounted for by the P^2 dependence of n_a. Indeed, we find that $n_a^{wf} = 2$ for a power of 2.1 W. By projecting each diffraction-limited spot in the FOV in one CCD pixel, it is then possible to find whether any pixel in the CCD has a chelated molecule with high SNR (~20) in 1 ms (the last generation of CCD cameras features speeds in excess of 1,000 frames per second), and thus fast scanning is feasible.

The scanning methodology deserves also some comments. During the fabrication of the BTD, each of the MTEs will be scanned and a map of pixels will be recorded. The map will contain the position of the pixel and the intensity response in the deep-blue band (for example, a filter of (400, 425) nm) to the interrogation of the scanning laser operating at the nominal parameters. The initial scan will allow us to identify and reject defective MTEs and to veto any potential defective spots.

Under normal operation, when the DCT triggers the scan of a specific region, the system records the signal in each spot and compares it with the reference in the database, as well as with the running average computed in real time. This allows us to take into account any local variation of density in the MTEs, as well as fluctuations in the laser power, which

are controlled with very good precision. The systematic error that we obtain when simulating these parameters is small compared with the bulk effect of the subtraction of the light that is due to unchelated molecules. Setting a very high nominal SNR (20 in our analysis) also provides extra protection against spurious fluctuations, which in our analysis never yielded an SNR greater than 3. To conclude, we think that a robust and reliable TPA scanning system can be implemented.

Data availability

The data that support the findings of this study are available within the paper and Supplementary Information. Additional data generated during the present study are available from the corresponding authors upon reasonable request.

47. Benesi, H. A. & Hildebrand, J. H. A spectrophotometric investigation of the interaction of iodine with aromatic hydrocarbons. *J. Am. Chem. Soc.* **71**, 2703–2707 (1949).
48. Zhang, Q. & Duan, K. Fluorescence chemosensor containing 4-methyl-7-coumarinyloxy, acetylhydrazono and n-phenylaza-15-crown-5 moieties for K+ and Ba^{2+} ions. *Heterocycl. Commun.* **24**, 141–145 (2018).
49. Batsanov, S. S. Van der Waals radii of elements. *Inorg. Mater.* **37**, 871–885 (2001).
50. Xu, C. & Webb, W. W. Measurement of two-photon excitation cross sections of molecular fluorophores with data from 690 to 1050 nm. *J. Opt. Soc. Am. B* **13**, 481–491 (1996).
51. Zinter, J. P. & Levene, M. J. Maximizing fluorescence collection efficiency in multiphoton microscopy. *Opt. Express* **19**, 15348–15362 (2011).
52. Denk, W., Strickler, J. H. & Webb, W. W. Two-photon laser scanning fluorescence microscopy. *Science* **248**, 73–76 (1990).
53. Byrnes, N. K. et al. Barium tagging with selective, dry-functional, single molecule sensitive on-off fluorophores for the NEXT experiment. In *Meeting of the Division of Particles and Fields of the American Physical Society* https://www.slac.stanford.edu/econf/C1907293/ (2019).
54. Amor, R. et al. Widefield two-photon excitation without scanning: Live cell microscopy with high time resolution and low photo-bleaching. *PLoS One* **11**, e0147115 (2016).

Author contributions J.J.G.-C., F.P.C. and D.N. conceived the project. J.J.G.-C and F.P.C. coordinated the experiments and analysed the data. I.R. and B.A. carried out the chemical synthesis, characterization and solution fluorescence studies of the compounds. J.I.M. carried out the NMR experiments. C.T., F.P.C. and D.C. performed the computational studies. P.H. and C.R. designed and performed the chelation in dry medium. Z.F. carried out the fluorescence studies in the silica experiments. B.O. and T.S. performed the solid-phase experiments involving polymers. J.M.B., R.M.M.-O., P.H., F.M. and P.A. performed the laser experiments (coordinated by J.M.B.). J.J.G.-C and F.P.C. wrote the manuscript. D.N., F.M., C.R. and Z.F. assisted in writing and editing the manuscript.
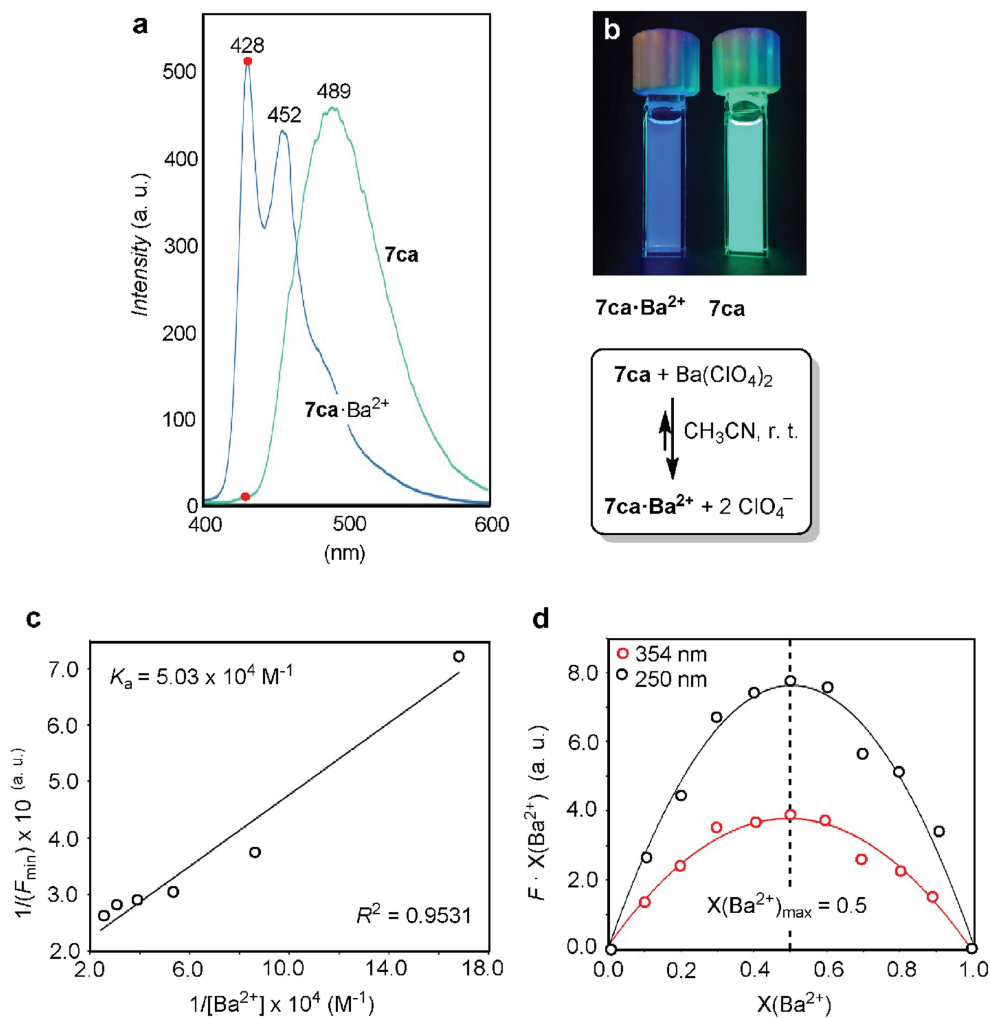
Extended Data Fig. 1 | Characterization of FBI in solution. a, Emission spectra of unchelated (**7ca**; cyan) and chelated (**7ca**Ba^{2+}; blue) indicators upon excitation at 250 nm. Red dots indicate the wavelengths used to determine the peak discrimination factor f_λ. **b**, Photographs of the two species in acetonitrile showing bicolour emission upon irradiation at 365 nm. **c**, Benesi–Hildebrand plot of the fluorescence emission spectra of FBI in acetonitrile solution at room temperature in the presence of different concentrations of barium perchlorate. **e**, Job's plot of the **7ca** + Ba(ClO$_4$)$_2$ interaction, showing a 1:1 stoichiometry between **7ca** and Ba^{2+}, thus forming the complex **7ca**Ba^{2+}. ΔF, variation in the measured emission; X(Ba^{2+}), molar fraction of Ba^{2+}.
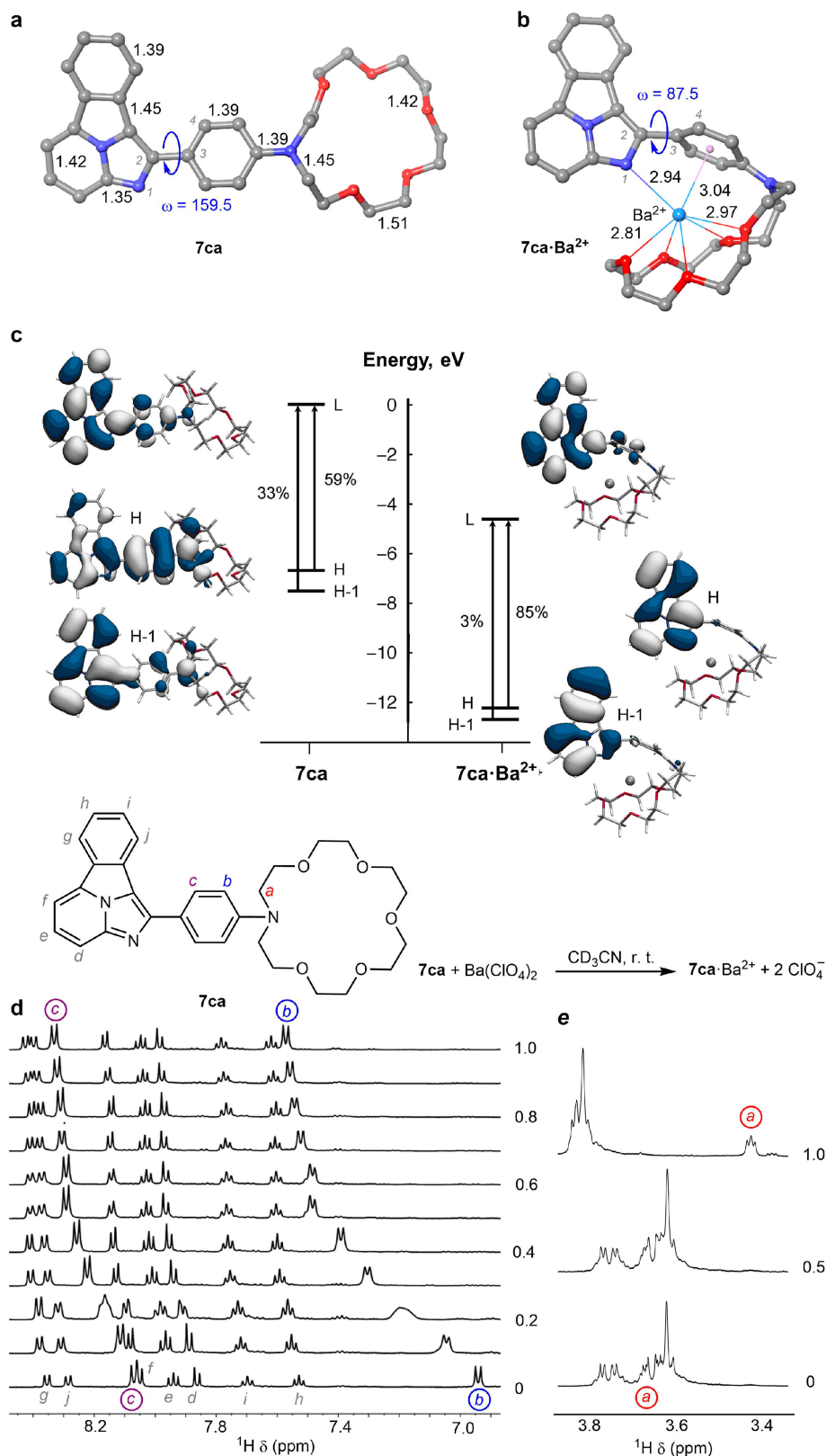
**Extended Data Fig. 2 | Theoretical predictions and NMR experiments.**
a, **b**, DFT-derived gas-phase structures of **7ca** (**a**) and **7ca**Ba²⁺ (**b**). Bond distances are given in Å. Dihedral angles ω formed by covalently bonded atoms 1–4 are given in degrees and in absolute values. **c**, Frontier molecular orbital energy diagram of **7ca** (left) and **7ca**Ba²⁺ (right). Vertical arrows indicate the main contributions to the electronic transition to the lowest bright state. **d**, **e**, Aromatic (**d**) and aza-crown ether (**e**) regions of the proton NMR spectra of

compound **7ca** upon addition of barium perchlorate. The most important changes in chemical shift (in ppm) are highlighted. All the spectra were recorded at 500 MHz. Protons *a* correspond to the methylene groups of the aza-crown ether moiety (**e**). Protons *b* and *c* (**d**) correspond to the para-benzylidene group. See the drawing of **7ca** in **d** for the assignment of all protons.
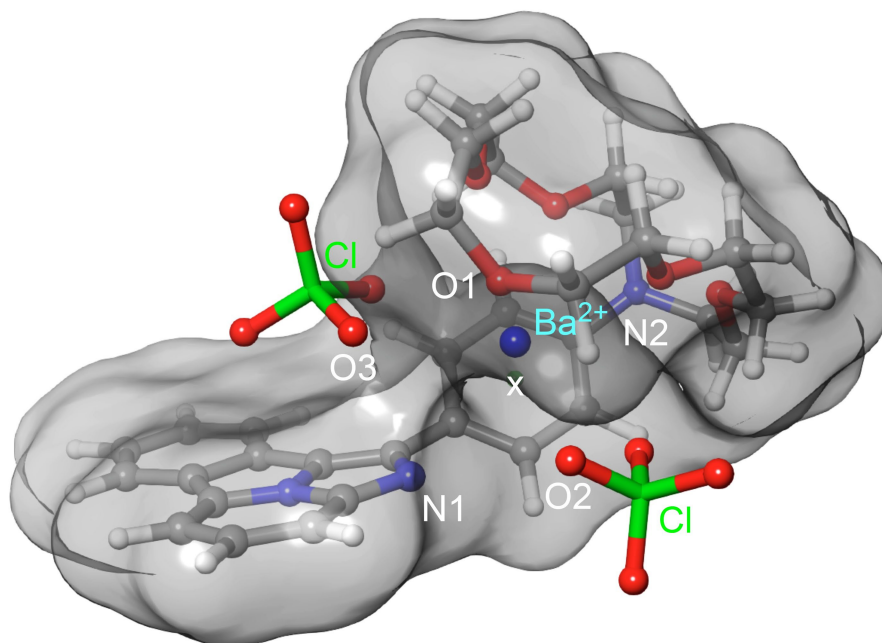
Extended Data Fig. 3 | Computed structures of FBI–barium perchlorate complex. DFT-derived fully optimized structure of **7ca** complexed with barium perchlorate. A dummy atom located at the centre of the 1,4-disubstituted phenyl group is denoted as X. Bond distances and dihedral angles are given in Extended Data Table 2.
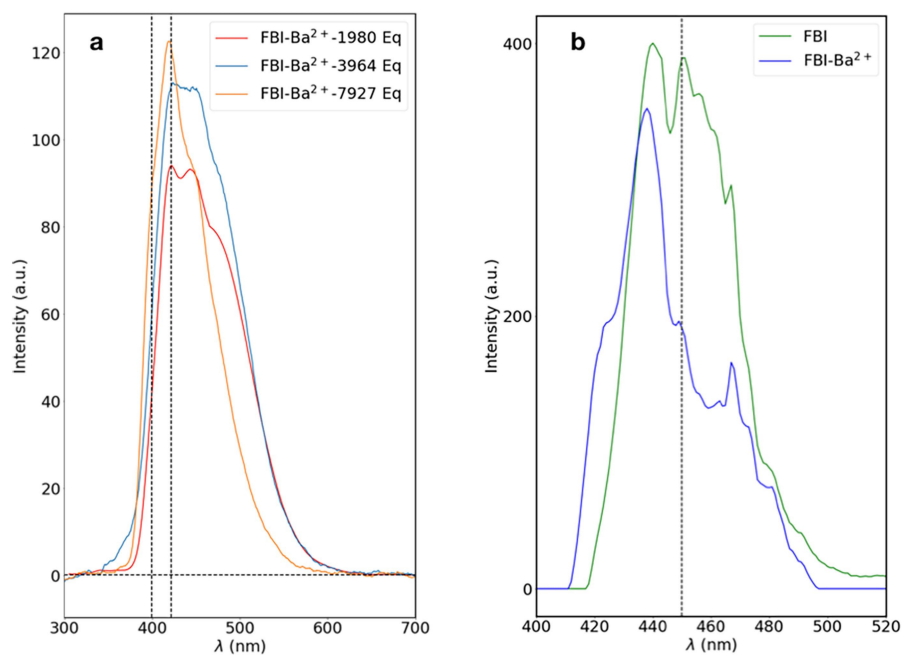
Extended Data Fig. 4 | Titration and polymer experiments. a, Titration experiments, showing that the response of the FBI improves for larger concentrations of barium. Eq, equivalent. **b**, Example of a polymer experiment, showing that the response of the FBI loses its characteristic colour shift.
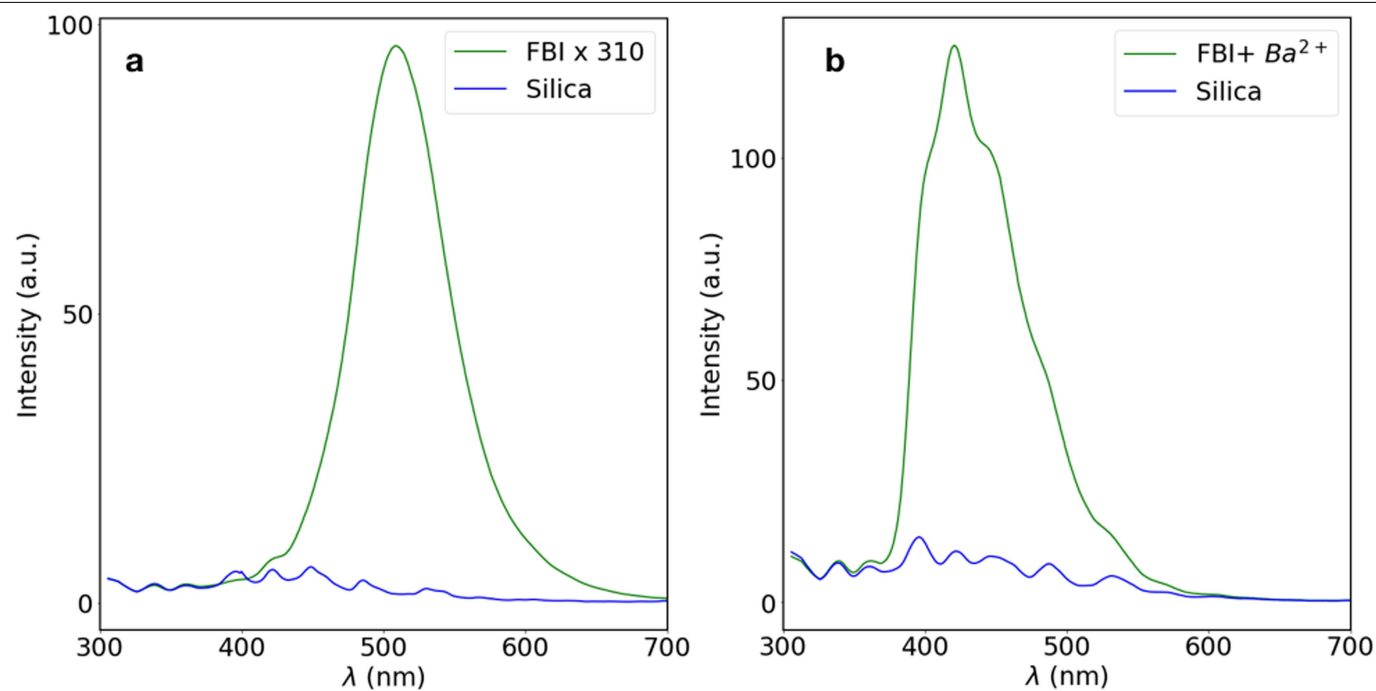
Extended Data Fig. 5 | Subtraction of the silica response. a, b, Emission spectra of the SF (**a**) and SBF (**b**) samples, with the background from the silica superimposed, for an excitation light of 250 nm.
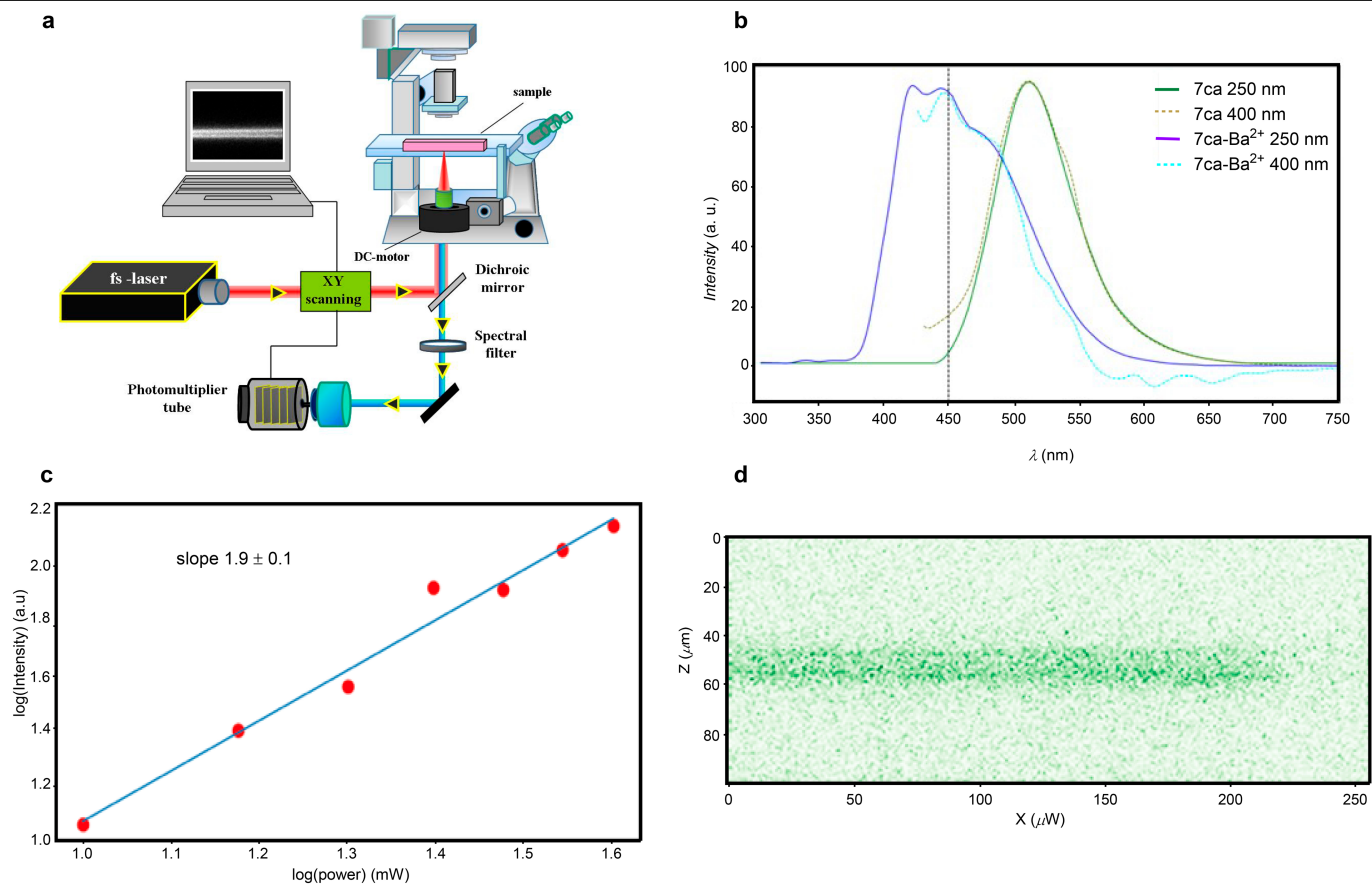
Extended Data Fig. 6 | TPA microscopy. a, Illustration of our setup. An infrared (800 nm) laser passes through a dichroic mirror and fills the back plane of the objective (20×, NA = 0.5) of an inverted microscope. The laser is focused in the sample, with a spot limited by diffraction (for example, a volume of about 1 μm³). The emitted fluorescence passes through a selection filter before being recorded by a PMT. **b**, Emission spectra of FBI and FBI Ba²⁺ for an excitation light of 250 nm (green, blue) and 400 nm (olive, cyan). The spectra are very similar, allowing the use of an infrared laser of 800 nm for our proof-of-concept study. **c**, Log–log plot showing the quadratic dependence of the intensity on the power, which is characteristic of TPA, for the FRS. **d**, Two-dimensional scan (profile) across the FRS. Integration of the profile yields an integrated signal that can be used for the normalization of the FBI samples.
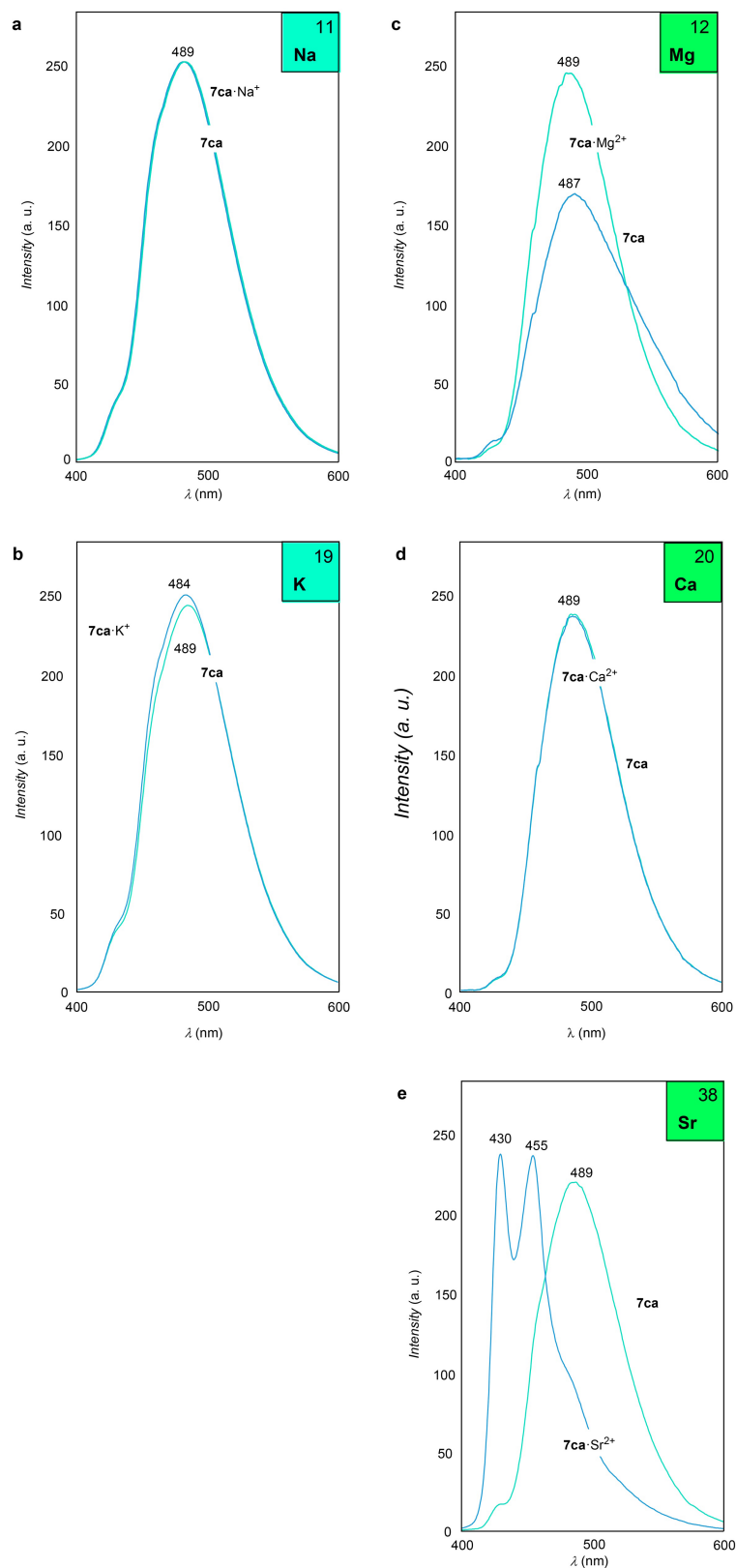
Extended Data Fig. 7 | Interaction of FBI with other elements (1:1 equiv.). a–e, Blue lines represent FIB + Na$^+$ (**a**), FIB + K$^+$ (**b**), FIB + Mg^{2+} (**c**), FIB + Ca^{2+} (**d**) and FIB + Sr^{2+} (**e**), and the cyan lines show the corresponding unchelated indicators. In **a–d**, the spectra show that the FIB is not chelated with the ion, whereas in **e** the response is similar to that observed for barium, showing the formation of a supramolecular complex. All excitation spectra were taken at 250 nm.
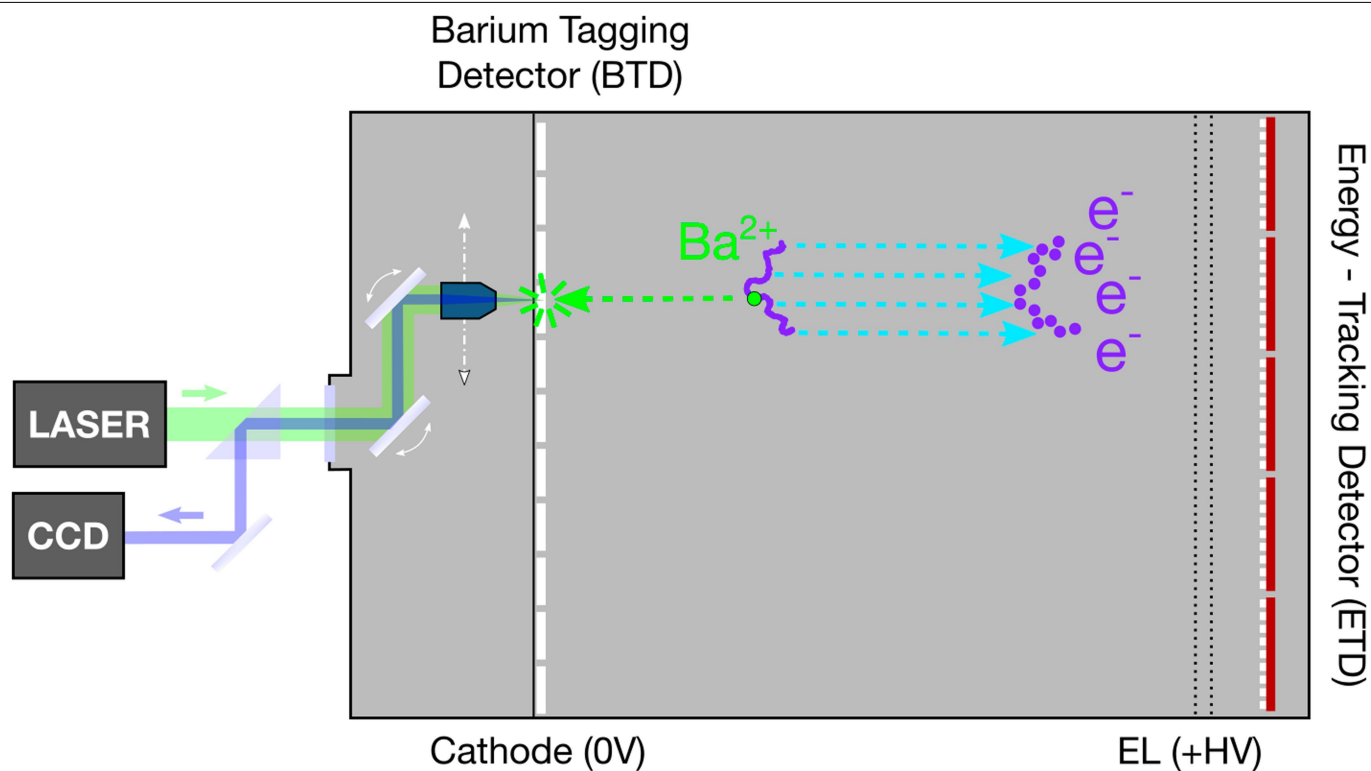
Extended Data Fig. 8 | Schematic of the BOLD detector. An example of a $\beta\beta0\nu$ signal event is shown. The two electrons emitted in the decay (purple) propagate in the dense xenon gas ionizing it, and the ionization electrons drift towards the anode, where their energy is measured by the ETD, which also reconstructs the event barycentre. The Ba^{2+} ion drifts very slowly towards the cathode, where it is eventually captured and identified by the BTD.

Extended Data Table 1 | Characterization of FBI compounds 7 and 7Ba^{2+}

Compound	λ_{em} [a] (nm)		f_λ [b]	ϕ_λ [c]		B_λ [d] (M^{-1}cm^{-1})	
	7	7—Ba^{2+}	7—Ba^{2+}	7	7—Ba^{2+}	7	7—Ba^{2+}
7aa	485	485	0.07	0.42	0.41	8.42	8.45
7ba	482	428	6.02	0.34	0.32	7.65	8.13
7ca	489	428	179.74	0.67	0.45	11.26	8.06
7da	491	491	n. d.	0.06	0.06	0.53	0.51
7ec	511	430	22.64	0.29	0.25	3.65	3.05
7cb	503	456	4.86	0.22	0.04	4.84	1.21

[a]Emission wavelengths (λ_{em}) at an excitation wavelength of 250 nm.
[b]Peak discrimination factors (f_λ) with respect to unbound fluorophores **7** at λ_{em}. n. d., not determined.
[c]Quantum yields (ϕ_λ) at λ_{em}.
[d]Molecular brightness of the fluorescent emissions (B_λ) at λ_{em}.

Extended Data Table 2 | Structural parameters for the geometries of 7caBa²⁺ and 7caBa(ClO₄)₂

$7ca \cdot Ba^{2+}$	$\omega B97X\text{-}D^a$	$B3LYP\text{-}D3^b$
$Ba^{2+}\text{-}O1^c$	2.84	2.87
$Ba^{2+}\text{-}N1^c$	2.92	2.94
$Ba^{2+}\text{-}N2^c$	3.82	3.91
$Ba^{2+}\text{-}X^c$	3.03	3.04
ω^d	82.9	76.3

$7ca \cdot Ba(ClO_4)_2$	$\omega B97X\text{-}D^a$	$B3LYP\text{-}D3^b$
$Ba^{2+}\text{-}O1^c$	2.84	2.85
$Ba^{2+}\text{-}O2^c$	2.79	2.90
$Ba^{2+}\text{-}O3^c$	2.94	2.96
$Ba^{2+}\text{-}N1^c$	3.04	3.14
$Ba^{2+}\text{-}N2^c$	4.15	4.53
$Ba^{2+}\text{-}X^c$	3.20	3.59
ω^d	45.0	43.1

The atomic labels are shown in Extended Data Fig. 3.
[a]Structures optimized in vacuo using DFT.
[b]Structures optimized in vacuo using DFT.
[c]Bond distances in Å.
[d]Dihedral angles (absolute value) are given in degrees.

Extended Data Table 3 | Gibbs reaction energies of compound 7ca with Ba²⁺ under different conditions

Reaction	Pressure (atm)	ΔGr_{xn}[a] (kcal/mol)
$\mathbf{7ca} + Ba^{2+} \rightarrow \mathbf{7ca}{-}Ba^{2+}$	1	-197.5
	10	-198.8
	20	-199.2
	30	-199.5
$\mathbf{7ca} + Ba^{2+}{-}8Xe \rightarrow \mathbf{7ca}{-}Ba^{2+}{+}8Xe$	1	-195.9[b]
$\mathbf{7ca} + Ba(ClO_4)_2 \rightarrow \mathbf{7ca}{-}Ba(ClO_4)_2$	1	-80.0

[a]ΔG_{rxn} is the free energy of the reaction, calculated as $\Delta G_{rxn} = \Sigma G_{prod} - \Sigma G_{react}$ (ΣG_{prod}, total free energy of the product; ΣG_{react}, total free energy of the reactants) at a temperature of 298.15 K and computed using DFT.

[b]Free energy of the reaction, computed considering isolated **7ca**Ba²⁺ clusters and eight individual Xe atoms as reaction products.